

# Synergetic regulation of hydration and carbonation of reactive MgO cement by amino acids

Shuang Liang<sup>a</sup>, Xiangming Zhou<sup>a,\*</sup>, Pengkun Hou<sup>a,b</sup>

<sup>a</sup> Department of Civil & Environmental Engineering, Brunel University London, Uxbridge, Middlesex UB8 3PH, United Kingdom

<sup>b</sup> Shandong Provincial Key Lab for the Preparation & Measurement of Building Materials, School of Materials Science & Engineering, University of Jinan, Jinan 250022, China

## ARTICLE INFO

### Keywords:

MgO  
Amino acids  
Carbonation  
Hydrated magnesium carbonates  
Polymorph control

## ABSTRACT

This study investigates the role of L-aspartic (L-Asp) in regulating the crystallisation of hydrated magnesium carbonates (HMCs) in carbonation-cured reactive MgO (RM). The effects of L-Asp on hydration kinetics, bulk density, compressive strength, phase composition, carbon sequestration, microstructure and morphology of RM composites were examined to understand its influence on the coupled hydration and carbonation processes. It has been found that L-Asp delays the precipitation of  $Mg^{2+}$  and  $OH^-$ , promoting the formation and stabilisation of the metastable nesquehonite ( $MgCO_3 \cdot 3H_2O$ ) polymorph. Carbonated composites incorporating L-Asp demonstrate a higher carbonation degree and enhanced stability compared to those without L-Asp. Notably, samples containing 0.2 M L-Asp sequestered 46.7 % more  $CO_2$  than those without amino acids. Additionally, amino acids lead to denser carbonation products with modified morphology, significantly enhancing carbonation efficiency and compressive strength. This study unveils the synergetic mechanism by which L-Asp influences hydration and carbonation in MgO-based binders, contributing to their enhanced performance.

## 1. Introduction

Concrete is one of the most widely used materials in the construction industry due to its abundance and excellent engineering properties. Its primary constituent, which acts as the binder to other constituents, is Portland Cement (PC). The conventional method of producing Portland cement involves calcining raw materials (i.e. clay and limestone) at high temperatures (up to 1400 °C). This process, combined with fuel consumption during the thermo-chemical process of calcination, releases a significant amount of carbon dioxide. Approximately 800–900 kg of carbon dioxide is released per tonne of PC produced [1,2], which contributes to 2–3 % of global primary energy consumption and 5–7 % of worldwide anthropogenic carbon dioxide emission [3].

Compared to CaO, which contributes 60–70 wt% of cement clinker, reactive MgO (RM) derived from  $MgCO_3$  calcination has a lower firing temperature (700–900 °C vs. 1450 °C for  $CaCO_3$ ) and is fully recyclable after its lifecycle [4,5]. Unlike PC-based mixes, RM-based binders gain strength through permanently sequestering  $CO_2$  via carbonation [6–9]. RM also offers superior mechanical properties and  $CO_2$  capture potential compared to PC-MgO blends. Additionally, the hydration and carbonation products of RM exhibit higher resistance to aggressive

environments, enhancing durability [10]. The hardening process of RM-based materials occurs through the reaction of magnesium-bearing materials with  $CO_2$  and moisture.

Thus, the magnesium-based binder has the potential to become an alternative cementitious material, which contributes to carbon sequestration [11,12]. When RM is used alone as the cementitious component, MgO hydrates to form brucite ( $Mg(OH)_2$ ), which provides minimal strength [13]. However, under suitable curing conditions, brucite reacts with  $CO_2$  and water to form hydrated magnesium carbonates (HMCs), which serve as the primary binding phases and enhance matrix strength. The main HMCs include nesquehonite ( $MgCO_3 \cdot 3H_2O$ ), hydromagnesite ( $4MgCO_3 \cdot Mg(OH)_2 \cdot 4H_2O$ ), artinite ( $Mg_2(CO_3)(OH)_2 \cdot 3H_2O$ ), and dypingite ( $4MgCO_3 \cdot Mg(OH)_2 \cdot 5H_2O$ ). These magnesium-based carbonates exhibit higher compressive strength than calcium-based binders, which are the primary binding agents in PC mixes [10]. Additionally, the magnesium-based carbonates also exhibit better cementing properties [14] and greater resistance to acid and sulphate attacks than calcium-based blends [15]. These advantages have fuelled growing interest in magnesia carbonation.

To maximise engineering applications of this novel cementitious material, it is highly important to understand its hydration and subse-

\* Corresponding author.

E-mail address: [Xiangming.Zhou@brunel.ac.uk](mailto:Xiangming.Zhou@brunel.ac.uk) (X. Zhou).

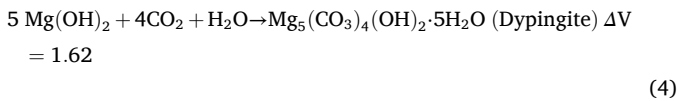
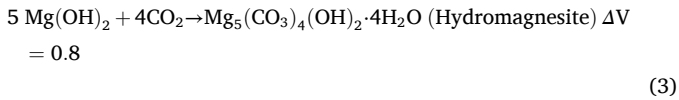
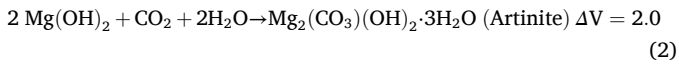
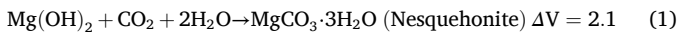
<https://doi.org/10.1016/j.cemconres.2025.107949>

Received 27 June 2024; Received in revised form 17 May 2025; Accepted 25 May 2025

Available online 28 May 2025

0008-8846/© 2025 The Author(s). Published by Elsevier Ltd. This is an open access article under the CC BY license (<http://creativecommons.org/licenses/by/4.0/>).

quent carbonation mechanisms. The carbonation of MgO can be described as the subsequent carbonation of hydrated magnesium carbonates, as shown in Eqs. (1)–(4), where  $\Delta V = \frac{V_{\text{HMC}}}{V_{\text{Mg(OH)}_2}}$  is the volume expansion factor. The conversion from brucite to HMCs is an expansion process, increasing solid volume by a factor of 1.8–3.1, thereby reducing porosity and overall pore volume [16–18]. Additionally, the binding strength and morphology of the HMC crystals contribute to network formation. However, this conversion route of HMC polymorphs in carbonated magnesia composites is affected by various factors, including temperature [18–20], relative humidity [21,22], CO<sub>2</sub> concentration [16,21,23,24], CO<sub>2</sub> pressure [25–27], and carbonation duration [23,28,29]. The final performance of RM formulations depends on the rate and degree of carbonation, as well as the morphology of the resulting carbonate phases [13,17]. For example, nesquehonite contributes more to strength gain than dypingite and hydromagnesite. Previous studies [30,31] have proven that mixes with dense nesquehonite formations achieve higher strength than those dominated by dypingite or hydromagnesite. During the conversion of brucite to nesquehonite, which exhibits an elongated needle-like morphology, the solid volume expands by a factor of 2.34, reducing porosity and increasing stiffness. Therefore, controlling HMC polymorph formation is crucial for optimising strength.



Nesquehonite typically forms in alkaline soils, caves and as a weathering product of ultramafic rocks, existing as a low-temperature carbonate. However, its instability at temperatures above 50 °C presents a challenge, as it readily transforms into more thermodynamically stable HMCs, such as dypingite or hydromagnesite, which have a lower CO<sub>2</sub>:Mg ratio than nesquehonite [32–34]. Therefore, controlling HMC polymorph is crucial for enhancing the properties of magnesia-based composites.

A novel approach to regulating HMC polymorphism in carbonated magnesia composites involves the use of organic matrices. This strategy has been successfully applied to the CaCO<sub>3</sub> system to stabilise typically metastable amorphous calcium carbonate (ACC), aragonite, and vaterite polymorphs [35–38]. A recent study [39] demonstrated that amino acids, at varying concentrations, can effectively stabilise carbonates in calcium-based cementitious systems. Notably, L-Asp, at higher concentrations, has proven the most promising results after 145 h, stabilising approximately 52 % ACC, the most unstable carbonate that sequesters the most CO<sub>2</sub> among all HMCs, while reducing calcite formation to approximately 1 %. It has been found that a series of organic molecules are responsible for the nucleation, polymorphic selection, and crystal growth of the CaCO<sub>3</sub> in biominerals [40,41]. An ‘organic-inorganic’ hybrid phase with remarkable strength, toughness, and durability can also be obtained by controlling the crystallisation of inorganic CaCO<sub>3</sub> with organic molecules [42].

Building on these findings, this study hypothesises that amino acids can enhance the performance of magnesium carbonate composites by influencing HMC polymorphism. This hypothesis is supported by the similar solubility of MgCO<sub>3</sub> and CaCO<sub>3</sub>, both of which belong to the alkaline-earth carbonate family [43–45]. Despite this potential, very few

studies have investigated additives that can control the polymorphs or modify the morphologies of RMCs. This study aims to address this gap by investigating a practical approach that can control the polymorphs of HMCs in carbonated MgO through amino acids, representing a novel method that can facilitate the accelerated carbonation for RM under carbon dioxide curing [35]. The experimental findings presented in this study were designed to validate the above-stated hypothesis.

## 2. Experimental procedure

### 2.1. Materials

The reactive MgO (i.e. RM, a light-burnt MgO) used in sample preparation was sourced from Magnesia GmBH, Germany, with a purity exceeding 95 % by weight and a specific surface area (SSA) of 0.3 m<sup>2</sup>/g. An amino acid, L-aspartic (L-Asp) (C<sub>4</sub>H<sub>7</sub>NO<sub>4</sub>), employed for this study was acquired from Sigma Aldrich, United Kingdom.

### 2.2. Specimen preparation for testing

Two types of samples were prepared for studying the carbonation and hydration of MgO. The first type was thin sheet paste samples with a thickness of <2 mm, which were prepared to investigate the HMC polymorph formation and evolution during carbonation. The other type was cubic paste samples with dimensions of 20 × 20 × 20 mm<sup>3</sup>, which were employed for measuring compressive strength.

Based on our previous studies [31,46,47] and trial-and-error experiments, the performance of amino acids tends to improve with the increasing dosage. The most significant effect was observed at 0.1 M when comparing 0.05 M and 0.1 M amino acids solutions [46]. Additionally, L-Asp solution approaches saturation at 0.2 M. Therefore, in this study, two L-Asp-containing solutions (with a concentration of 0.1 M and 0.2 M, respectively) were prepared by dissolving dry L-Asp in deionised water. MgO powders were then manually mixed with these solutions for 5 min at a liquid (water or L-Asp solution)-to-binder (l/b) ratio of 0.8 by weight. A control group was prepared by mixing MgO with deionised water without amino acids. These pastes were spread onto a plastic film to form sheet samples with a thickness of <2 mm and then subjected to ambient curing and CO<sub>2</sub> curing, respectively. In the ambient curing regime, the samples were placed in an environmental chamber at 25 °C and a CO<sub>2</sub> concentration of 0.041 vol% to investigate the effects of L-Asp on the hydration of MgO. The relative humidity (RH) was maintained at 95 % to accelerate the hydration of MgO. The laboratory CO<sub>2</sub> curing regime adopted in this study is schematically illustrated in Fig. 1, in which an industrial-grade CO<sub>2</sub> gas with a purity of 95

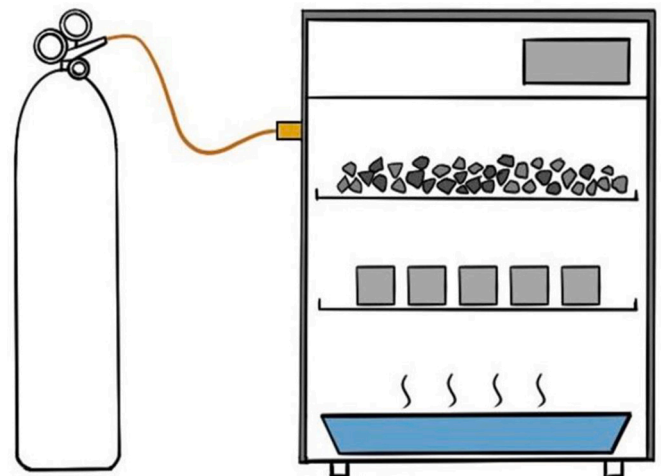


Fig. 1. Experimental setup of CO<sub>2</sub> curing.

% was used for curing the samples. The CO<sub>2</sub> pressure in the curing chamber was sustained at 1 bar for the designated carbonation duration. Throughout the carbon curing process, the CO<sub>2</sub> concentration, temperature, and relative humidity were maintained at (15 ± 0.5)%, (30 ± 1) °C, and (80 ± 5)%, respectively, in the chamber. The mix formulations and their curing regimes are presented in Table 1. Carbonated/hydrated pastes were removed from the chamber at intervals of 1, 3, 7, and 14 days. Then the samples were placed in isopropanol for another 7 days to arrest the hydration. Subsequently, the samples were dried at 30 °C to remove the solvent and then milled into powder using a mortar pestle.

RM paste with an l/b ratio of 0.8 by weight was prepared and cast into 20 × 20 × 20 mm<sup>3</sup> cubic moulds. Immediately after casting, the cubic samples in moulds were placed for 1 day in the same carbonation chamber employed for curing thin paste samples. Then the cubic samples were de-moulded and remained in the carbon chamber until reaching the designated testing ages.

## 2.3. Methodology

### 2.3.1. pH measurement

The paste samples were ground into fine powders to measure their pH at different time intervals, using a calibrated Mettler Toledo pH meter with an accuracy of ±0.01, following ASTM C25-19 [48]. Before each measurement, the pH meter was calibrated by immersing a clean electrode in a neutral pH 7.00 buffer solution and allowing the reading to stabilise. The electrode was then rinsed with distilled water and recalibrated using a second buffer solution (pH 10.01). To measure pH, a solution of 5 g of powder mixed with 100 g of distilled water was prepared in a sealed container. The mixture was stirred continuously for 30 min before measurement. To minimise environmental influences, all measurements were conducted in a temperature-controlled room, as pH values are temperature-sensitive. Additionally, to limit sample exposure to atmospheric CO<sub>2</sub>, all samples were stored and mixed in sealed containers. While potential sources of error cannot be eliminated, each measurement was performed six times, and the average value was reported as the representative pH to mitigate possible errors. The hydroxide ion (OH<sup>-</sup>) concentration was calculated using Eqs. (5)–(6).

$$\text{pH} = -\log [\text{H}^+] \quad (5)$$

$$[\text{OH}^-] = \frac{10^{-14}}{[\text{H}^+]} \quad (6)$$

### 2.3.2. XRD, FTIR, TG/DTG and SEM-EDX

The XRD patterns of all samples were obtained using a Bruker D8-Advance X-ray diffractometer equipped with Cu K $\alpha$  radiation ( $\lambda = 1.5418 \text{ \AA}$ ). The instrument operated at an operational voltage of 40 kV and a current of 40 mA, with a scanning rate of 0.02° 2 $\theta$  /step over a range of 5 to 50° 2 $\theta$ . Fourier transform infrared (FTIR) analysis with spectral subtraction was performed using a Perkin Elmer fitted with a Specac Quest attenuated total reflectance (ATR) accessory. FTIR spectra were recorded in the band between 800 cm<sup>-1</sup> to 1350 cm<sup>-1</sup>, with a resolution of 2 cm<sup>-1</sup> and a scan count of 32 at a scanning rate of 5 kHz. TG/DTG analyses were conducted using a TA Instrument TGA 4000. Samples were heated from 20 to 1000 °C at a rate of 10 °C /min under a nitrogen atmosphere. The microstructure and the morphology of HMCs

**Table 1**  
Mix formulations of MgO samples and curing regimes.

Group	MgO	L-Asp	l/b ratio	Curing regimes
C-A	100 %	0	0.8	Ambient curing
0.1 M-A	100 %	0.1 M	0.8	Ambient curing
0.2 M-A	100 %	0.2 M	0.8	Ambient curing
C-C	100 %	0	0.8	CO <sub>2</sub> curing
0.1 M-C	100 %	0.1 M	0.8	CO <sub>2</sub> curing
0.2 M-C	100 %	0.2 M	0.8	CO <sub>2</sub> curing

were examined using secondary electron (SE) images with a Zeiss Supra 35VP SEM. Before SEM analysis, samples were broken into smaller pieces and then dried for a few days to remove residual moisture. The dried samples were then mounted on metal stubs using carbon tape and subsequently sputter-coated with gold to enhance conductivity before being examined by SEM.

### 2.3.3. Compressive strength

The cubic samples cured in the carbonation chamber were subjected to compression testing at 1, 3, 7 and 14 days at a loading rate of 0.4 MPa/s in line with ASTM C109/C109M-13 [49]. The average of the strengths of three samples of the same formulation, age and carbonation curing was taken as the representative strength of the corresponding mixture.

### 2.3.4. Hydration heat

The effect of L-Asp on the hydration kinetics of MgO pastes was evaluated using isothermal calorimetry. Each batch consisted of 5 g of samples (containing 2.8 g of MgO and 2.2 g of water), which were placed in a glass ampoule and subsequently loaded into an isothermal calorimeter (TAM Air, Thermometric AB, Sweden). As the temperature was set at 25 °C, the heat flow under this temperature was monitored to investigate the effects of L-Asp on the hydration kinetics of MgO.

### 2.3.5. Ion concentration

The samples were categorised into three groups: C-A, 0.1M-A and 0.2M-A, mixed at an l/b ratio of 0.8. The prepared mixture was then loaded into centrifuge tubes. Three tubes were allowed to stand for 1, 3, 5, 7, 9 and 11 h, respectively. After the designated time intervals, the supernatant was collected and filtered through a 0.22  $\mu\text{m}$  filter to obtain the original solution. To ensure that the ion concentration was distributed as far as possible in the standard curve range, the original solution was diluted 100-fold, and the concentration of Mg<sup>2+</sup> in the diluted solution was then measured using inductively coupled plasma emission spectrometry (ICP-OES, Perkin Elmer Optima 2100 DV).

## 3. Results and discussion

### 3.1. Hydration

#### 3.1.1. XRD

Fig. 2 shows the XRD patterns of MgO matrices hydrated for 14 days, with and without amino acids. Regardless of the presence of amino acids, all samples exhibited brucite (Mg(OH)<sub>2</sub>) and unreacted MgO (Periclase) phases. It should be noted that even without carbonation curing, there was still a small amount of HMCs (i.e. 29.5° 2 $\theta$ ) formed in the samples, which can be attributed to the reaction between MgO and atmospheric CO<sub>2</sub>. The intensity of brucite peaks decreased with the increasing L-Asp concentration at all hydration ages, suggesting that L-Asp inhibited the hydration of MgO. Little MgO phase was present in the mixtures after 14 days, suggesting that the samples were mostly hydrated. Another interesting finding is that the intensity of brucite peaks was still low in L-Asp-containing samples, while the periclase (MgO) peaks were negligible in all groups after 7 days, suggesting that there was a very limited amount of brucite formed in the samples containing L-Asp, though MgO was highly dissolved. Moreover, the amorphousness of brucite increased with the increasing L-Asp concentration, as observed across all curing regimes, where the brucite peaks became broader as the concentration of L-Asp increased. Compared to the control samples, the L-Asp-containing samples had lower amounts of brucite content with reduced crystallinity, which could be attributed to the combination of the negatively charged L-Asp molecules and Mg<sup>2+</sup> [47].

#### 3.1.2. pH value

The measured pH values and OH<sup>-</sup> concentration of the sample suspensions are presented in Fig. 3. Since pH is a logarithmic scale, even a

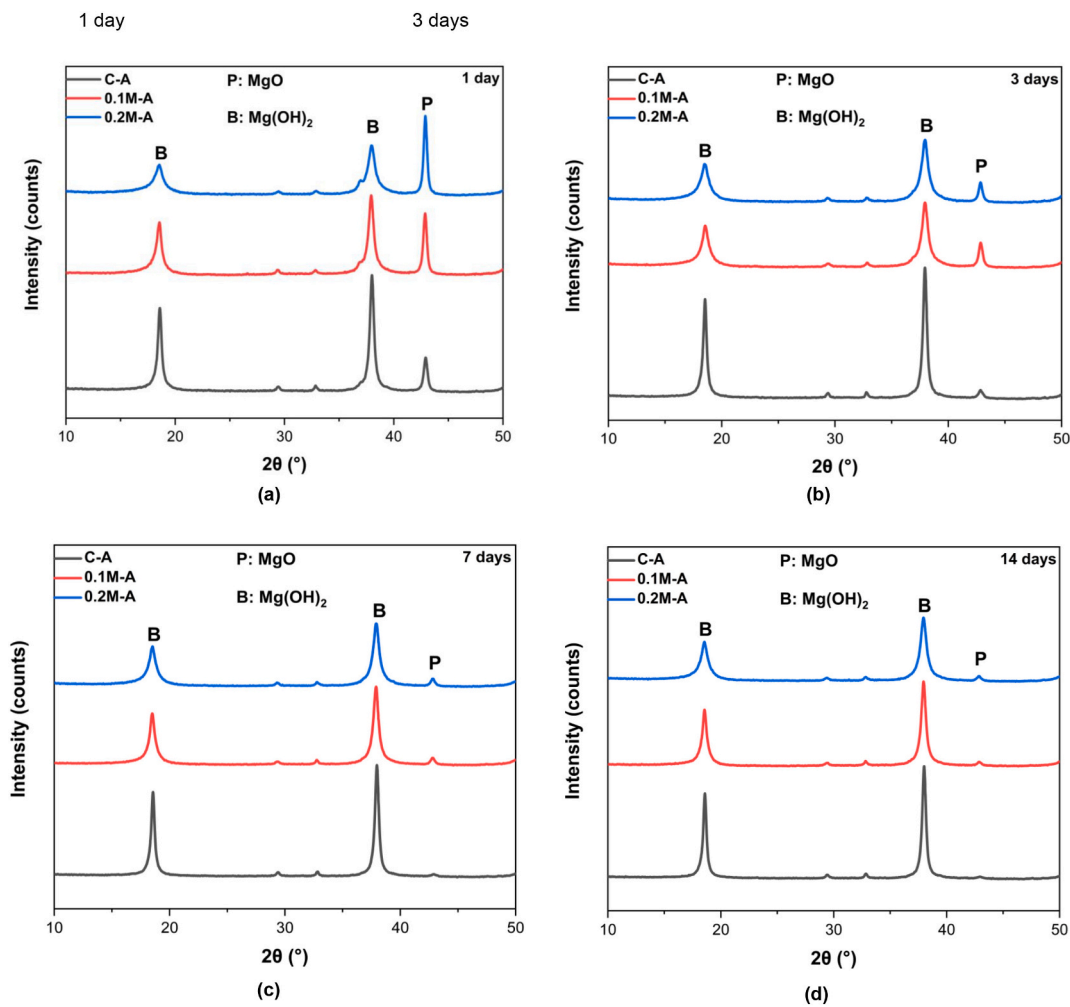


Fig. 2. X-ray Diffraction patterns showing the effects of L-Asp on MgO hydration after (a) 1, (b) 3, (c) 7, and (d) 14 days of ambient curing (B: Brucite ( $Mg(OH)_2$ ); P: Periclase ( $MgO$ )).

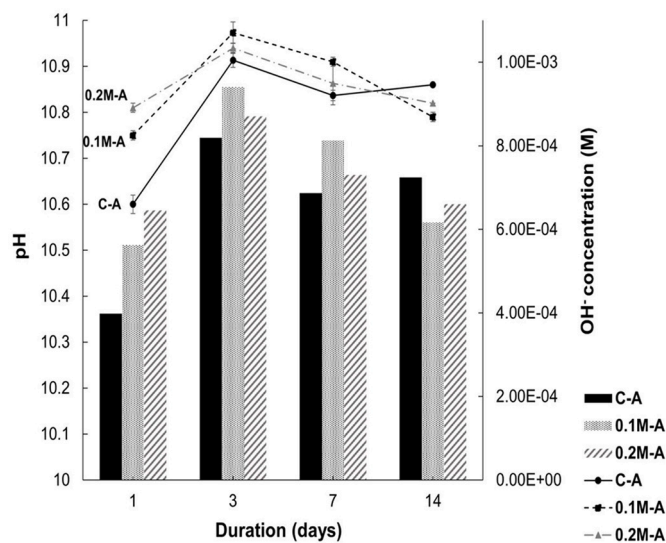


Fig. 3. pH values and  $OH^-$  concentration of all sample suspensions at 1, 3, 7, and 14 days (Lines correspond to pH values; Columns correspond to  $OH^-$  concentration).

0.1-unit difference corresponds to approximately a twofold change in hydroxide ion concentration. Given the minor variations in pH observed in this study,  $OH^-$  concentration was calculated as a supplementary result to further illustrate the anionic conditions within the binder. The small error bars across all samples reinforce the reliability of the data presented. L-Asp retarded the precipitation of  $OH^-$  ions (Fig. 3), consequently, increased the concentration of hydroxide ions, creating a weak alkaline environment, and thus a higher pH value was observed in the L-Asp-containing samples compared to the C-A samples. The most distinction was observed on the first day, where the pH of the 0.2 M-A sample was 0.21 units higher than that of the C-A sample, suggesting that the most effective period of L-Asp was the first day and the best opportunity to carbonate the L-Asp containing MgO binder was the first day of curing, as the highest pH value can benefit the dissolution of  $CO_2$  within the binder. However, at 14 days, the 0.1 M-A and 0.2 M-A samples demonstrated lower pH values than the C-A sample, which could be attributed to L-Asp depletion over time.

### 3.1.3. Hydration heat

Fig. 4 presents the heat flow released during the first 72 h of hydration for all samples. Fig. 4(a) illustrates that the cumulative heat curve of the MgO sample slowed down when approaching 36 h of hydration, while that of the other two groups of samples kept increasing, suggesting the retardation of the hydration when L-Asp was added. According to XRD results (presented in Section 3.1.1),  $Mg(OH)_2$  was the only hydration product formed in the pastes under ambient curing,

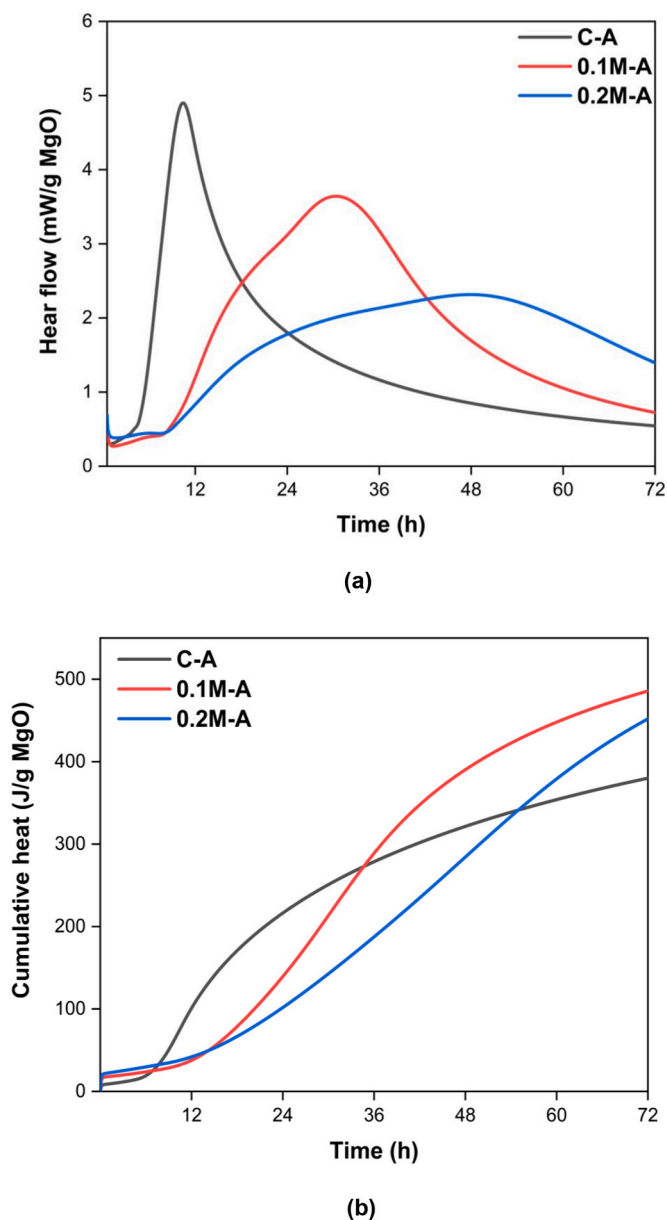


Fig. 4. (a) Heat flow and (b) cumulative heat of MgO paste samples with L-Asp under ambient curing.

therefore, the heat release of the sample was ascribed to the hydration of MgO, regardless of the presence of L-Asp. L-Asp led to a two-stage hydration process in samples with 0.1–0.2 M L-Asp. The first stage of hydration displayed pre-induction peaks associated with the dissolution of RM and subsequent precipitation of brucite, which occurred during the first ~10 h of hydration. These pre-induction peaks, partially attributed to the endothermic reactions of the hydrolysis of L-Asp, were lower than the peaks of the C-A samples. The low level of pre-induction peaks also indicated that the dissolution of RM in samples using the L-Asp mixture was low because of their higher initial pH when compared to that of the C-A samples. Between the two hydration stages, an induction period occurred, during which the dissolved ions reached the critical concentration to form the hydration products. The second stage was the acceleration and deceleration phases associated with the increase in heat released from the nucleation, growth, and precipitation processes in hydration products. A higher L-Asp concentration was associated with higher endothermic reactions in the MgO-L-Asp solution, thereby causing a delay in the appearance of peaks in the acceleration-

deceleration phase.

Overall, samples C-A exhibited the most pronounced acceleration in hydration. The inclusion of 0.1 M or 0.2 M L-Asp in MgO blends increased the dormant period and shifted the main peak to a later stage (i.e. ~30 h for sample 0.1 M-A and ~47 h for sample 0.2 M-A vs. ~12 h for sample C-A), resulting in obvious retardation of hydration, which is line with the XRD results (Fig. 1). However, the broader hydration peaks observed in the samples containing L-Asp demonstrated the enhancement of the dissolution of MgO by introducing amino acids. Nevertheless, amino acids also delayed hydration by combining  $Mg^{2+}$  and  $OH^-$ , which will be further discussed in Section 4.

### 3.1.4. Ion concentration

Fig. 5 illustrates the variation in  $Mg^{2+}$  concentration in the solution over 1 to 11 h of hydration. As demonstrated in Fig. 3, both 0.1 M-A and 0.2 M-A samples contained more unreacted MgO than the control samples, indicating a lower dissolution of MgO (i.e. theoretically lower  $Mg^{2+}$  concentrations in the solution). However, higher  $Mg^{2+}$  concentrations were observed in 0.1 M-A and 0.2 M-A samples, compared to the C-A samples. This suggests that the presence of L-Asp significantly increased the concentration of  $Mg^{2+}$  in the solution by inhibiting the precipitation of brucite. The MgO hydration process began with MgO acting as an electron donor in water, releasing  $Mg^{2+}$  and  $OH^-$  ions into the solution (Eqs. (7)–(9)). Therefore, the  $Mg^{2+}$  concentration rose. However, the precipitation of magnesium hydroxide ( $Mg(OH)_2$ ) soon occurred on the surface of MgO particles, leading to a decrease in  $Mg^{2+}$  concentration. The negatively charged carboxyl surface sites of L-Asp bound with  $Mg^{2+}$  sites by sharing an electron [39]. Such a bond then inhibited further reaction between  $Mg^{2+}$  and  $OH^-$ , and prevented the formation of brucite, which explains the increased concentration of  $Mg^{2+}$  in the mixtures. Initially, the  $Mg^{2+}$  concentration of the 0.1 M-A sample was 7.7 times that of the C-A sample, while the concentration in the 0.2 M-A sample was 14 times that of the C-A sample. The  $Mg^{2+}$  concentration in all samples decreased after about 1 h of hydration because of the formation of brucite. However, the depletion of  $Mg^{2+}$  concentration occurred after approximately 4 h of hydration in the C-A sample, while the 0.1 M-A and 0.2 M-A samples maintained higher  $Mg^{2+}$  concentrations, suggesting that the formation of brucite was delayed by L-Asp, which agrees well with XRD and hydration heat results.

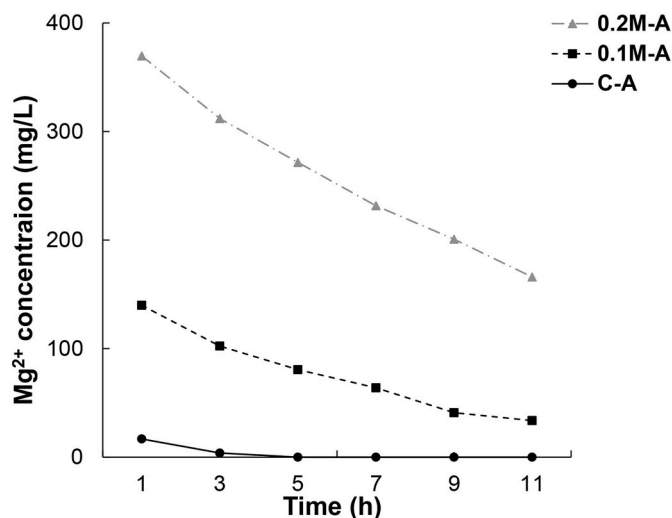
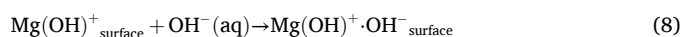


Fig. 5. Total  $Mg^{2+}$  concentration in suspension regarding hydration time for MgO in distilled water with/without L-Asp.



### 3.2. Carbonation

#### 3.2.1. Bulk density

The bulk density of the samples subjected to both ambient and CO<sub>2</sub> curing is presented in Fig. 6. Among the hydrated samples (i.e. C-A, 0.1 M-A, and 0.2 M-A), a decrease in density was noticed in the C-A sample at all curing ages, while the other samples exhibited relatively stable densities. These results suggest that the C-A sample experienced greater water evaporation than other samples, as the mass of the C-A sample was reduced by 5.3 % at 14 days compared to other samples. The contrary scenario was observed in the 0.1 M-A and 0.2 M-A samples after 3 days of curing, where their densities increased, which may be related to the favourable interactions between water and salt ions. Water in salt has a lower vapour pressure (i.e. it tends to evaporate slower), and this effect can be very apparent at high solute concentrations (i.e. 0.2 M of L-Asp) [50]. Therefore, the 0.2 M-A samples had the highest density from 1 to 14 days, as L-Asp increased the viscosity of the aqueous solution, resulting in a slower evaporation of water [51].

Concerning the samples subjected to CO<sub>2</sub> curing (Fig. 6), their bulk density was higher than that of the hydrated samples, which almost stabilised after the 3 days of CO<sub>2</sub> curing. The density of the C-C samples remained constant over time because of the formation of carbonate compounds that offset the decrease in density in the C-A samples that occurred at ambient temperatures. The rapid increase in the density from 1 to 3 days of CO<sub>2</sub> curing was exhibited in the 0.1 M-C and 0.2 M-C samples, corresponding to an increase of 10.1 % and 5.6 %, respectively. This is probably because more HMCs were formed, which comprised CO<sub>2</sub> and water in their chemical structures. However, even though all samples were under CO<sub>2</sub> curing, their densities still decreased after 3 days, which may be related to the evaporation of water [51]. Except for the water content, bulk density can also indirectly reflect the porosity of the samples. A higher bulk density indicates lower porosity because a greater proportion of the volume is taken up by solid components rather than voids. In this regard, L-Asp can reduce the porosity of magnesia-based samples, regardless of curing methods. This reduction in porosity may explain the increased compressive strength observed in the 0.2 M-C samples, as shown in Fig. 7.

#### 3.2.2. Compressive strength

Fig. 7 illustrates the strength development of all samples after 14 days of CO<sub>2</sub> curing. Despite a higher amount of HMCs being observed in the 0.1 M-C and 0.2 M-C samples at 1 day, which are revealed in XRD

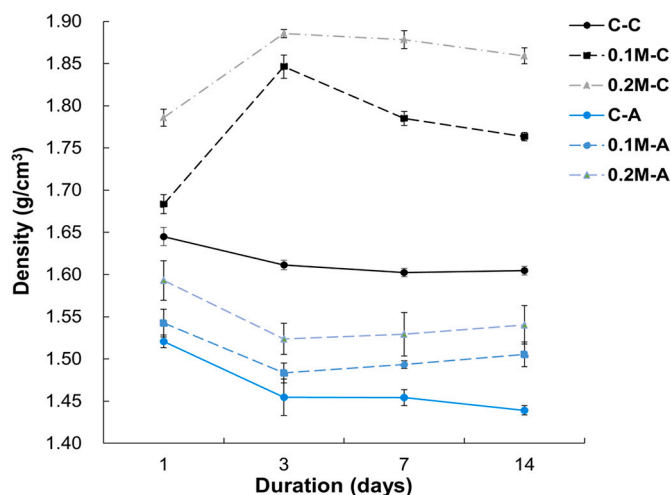


Fig. 6. Bulk density evolution of samples under ambient curing and CO<sub>2</sub> curing.

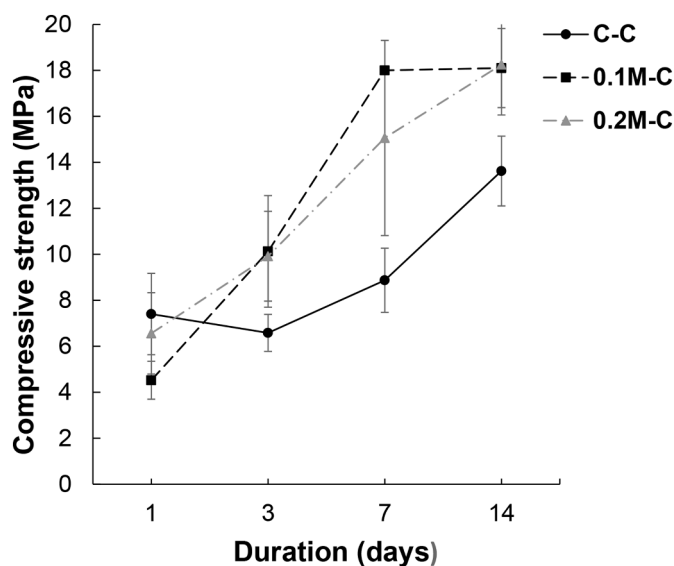


Fig. 7. Compressive strength of all samples under CO<sub>2</sub> curing up to 14 days.

and TG/DTG results, they both had lower strengths compared to the C-C sample (~7.4 MPa), suggesting that the mechanical strength of magnesium-based binder is contributed by both hydration and carbonation products [18,52]. Consequently, because of limited hydration, 0.1 M-C and 0.2 M-C samples only reached strengths of ~4.5 and ~6.6 MPa, respectively, at 1 day. It is also worth noting that the samples were kept in the moulds during the first day of curing, where carbonation can only occur on the top surface exposed to CO<sub>2</sub>. After 3 days of curing, the strength of both the 0.1 M-C sample and 0.2 M-C sample exceeded that of the C-C sample, reaching a comparable strength of ~10 MPa. The similar mechanical strengths of the 0.1 M-C and 0.2 M-C samples are ascribed to the comparable amount of hydration and carbonation products (i.e. brucite and nesquehonite), which agree well with the XRD patterns (Fig. 8). Notably, the use of smaller specimens (20x20x20 mm<sup>3</sup>) increased variability in compressive strength results. This sensitivity to local imperfections and stress distribution likely explains the larger error bars at 7 days. However, minor error bars before this point confirm the reliability of the trends observed. Despite these limitations, the overall strength enhancement supports the validity of the results and provides insights into the mechanical performance of the samples. The rapid development of compressive strength within the first 3 days could also be attributed to the efficiency of L-Asp, as evidenced in Fig. 3, where the highest pH value was achieved, which was desirable for the dissolution of CO<sub>2</sub> within the binder. Beyond this point, the strengths of the 0.1 M-C and 0.2 M-C samples were at least ~52.3 % and up to ~104.5 % higher than that of the C-C samples, suggesting that the content and polymorphs of HMCs played important roles in the strength development of magnesium-based binders.

The most notable strength improvement was observed in the 0.2 M L-Asp-containing samples, which increased by 177 % after 14 days of curing, ultimately reaching the highest strength (i.e. ~18.3 MPa). Compared to the C-C sample, the compressive strength of the 0.1 M-C and 0.2 M-C samples increased by 33 % and 35 %, respectively, after 14 days. Although the 0.1 M-C sample exhibited a 302 % strength increase over this period, its 1-day strength (~4.5 MPa) was significantly lower than that of the 0.2 M-C sample. Interestingly, the 0.1 M-C sample maintained the highest strength among all samples up to 7 days, despite not containing the highest HMC content, as shown in Fig. 8. This finding reinforces that, with comparable carbonation product formation, the mechanical strength of magnesium-based binders results from a synergistic effect of hydration and carbonation products. Ultimately, the 0.2 M-C sample achieved the highest compressive strength at 14 days due to its substantial HMC content. It should be noted that the samples were

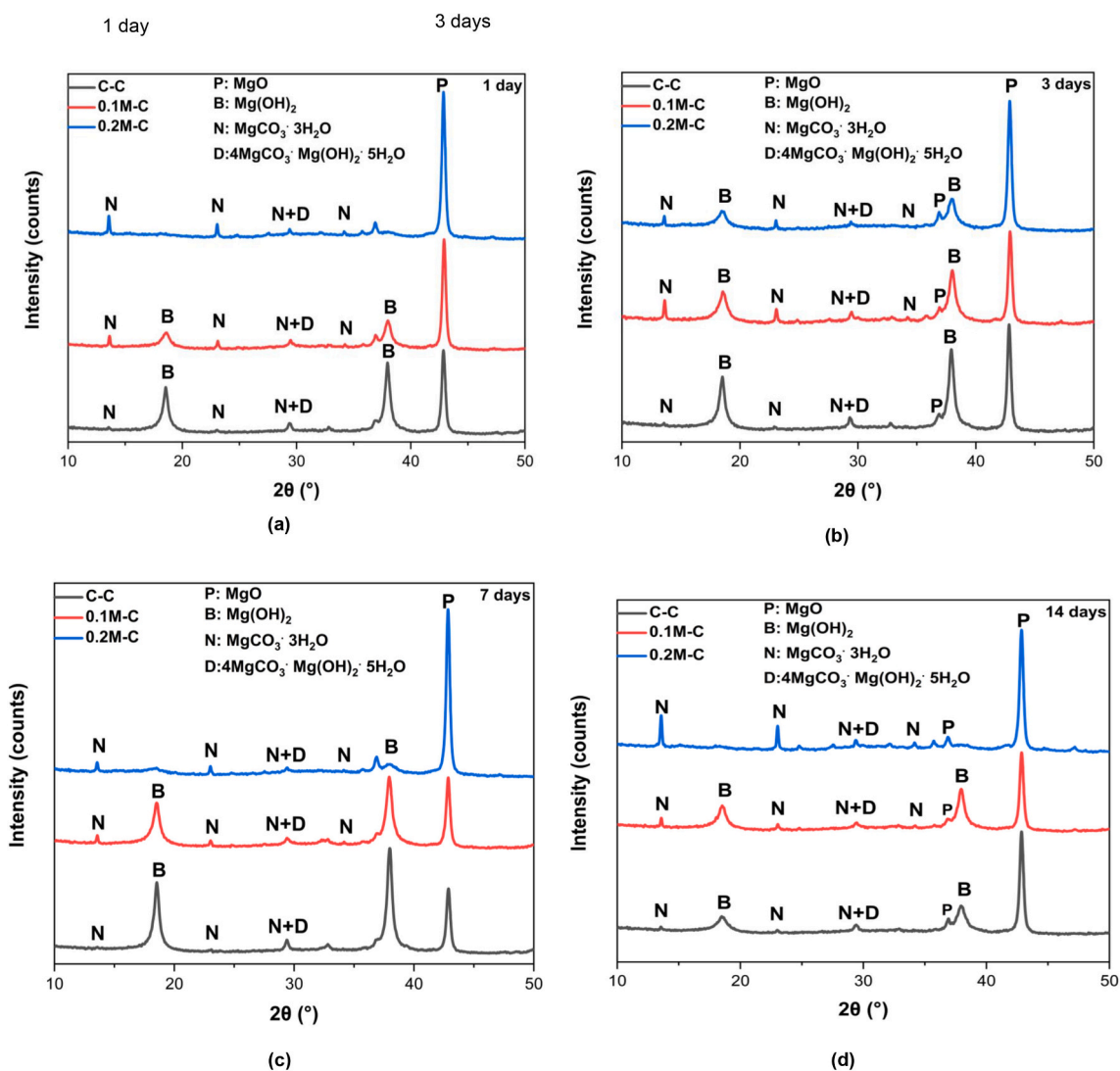


Fig. 8. XRD of all samples subjected to (a) 1; (b) 3; (c) 7; and (d) 14 days of carbonation curing (B: Brucite ( $\text{Mg}(\text{OH})_2$ ); N: Nesquehonite ( $\text{MgCO}_3 \cdot 3\text{H}_2\text{O}$ ); D: Dypingite ( $4\text{MgCO}_3 \cdot \text{Mg}(\text{OH})_2 \cdot 5\text{H}_2\text{O}$ ); P: Periclas ( $\text{MgO}$ )).

prepared with a high l/b ratio of 0.8 to ensure adequate flowability. Under optimised conditions with an ideal l/b ratio and additional additives, even higher strengths could be anticipated. For instance, MgO binder subjected to 7 days of carbonation curing at 100 %  $\text{CO}_2$  concentration reached up to 70 MPa [22].

Several key factors influenced the mechanical performance, including the quantity of formed products, which reduced porosity and densified the microstructures. However, based on the XRD patterns, the C-C and 0.1 M-C samples exhibited similar carbonation phase amounts at 14 days (Fig. 8), yet the 0.1 M-C samples demonstrated significantly higher strength than the C-C sample (i.e. 18.1 vs. 13.6 MPa). This discrepancy may be attributed to differences in the morphology of the carbonation products. Specifically, fibrous and needle-like crystallisations enhance strength more effectively than rounded or tabular crystals [53]. The interlocking effect of fibrous nesquehonite, owing to its 3D structure, contributed to higher compressive strength, explaining why L-Asp-containing samples outperformed C-C samples [53].

### 3.2.3. XRD

All samples exhibited the formation of HMCs, indicating carbonation during curing. Unhydrated MgO, identified by its main peak at  $42.9^\circ 2\theta$  in Fig. 8, was detected in all samples, regardless of L-Asp presence, suggesting incomplete MgO carbonation after 14 days. In contrast,

ambient-cured samples showed minimal periclas (i.e. unhydrated MgO) peaks, indicating nearly complete MgO reaction. The difference arises because unreacted MgO particles were encapsulated by hydration and carbonation products, limiting their exposure to  $\text{CO}_2$  and  $\text{H}_2\text{O}$  and thereby hindering further carbonation.

The peak at  $29.5^\circ 2\theta$  corresponds to HMCs, specifically nesquehonite ( $\text{MgCO}_3 \cdot 3\text{H}_2\text{O}$ ) and dypingite ( $4\text{MgCO}_3 \cdot \text{Mg}(\text{OH})_2 \cdot 5\text{H}_2\text{O}$ ), which were present in all samples across all curing ages. However, in C-C samples, nesquehonite peaks at  $13.5^\circ$ ,  $23^\circ$ ,  $34.5^\circ$ , and  $36^\circ 2\theta$  were negligible, suggesting that the primary carbonate was dypingite, a more thermodynamically stable form of magnesium carbonate. As nesquehonite transitions to more stable HMCs under high temperatures. In the C-C sample, nearly all nesquehonite had converted to dypingite, confirming its stability. Additionally, this peak (i.e.  $29.5^\circ 2\theta$ ) was most prominent after 14 days of curing in the control sample (C-C), indicating that dypingite remained the dominant HMC in the C-C sample over time.

Conversely, nesquehonite peaks were consistently present in amino acid-containing samples at all curing ages, but with different intensities. At 1, 7 and 14 days (see Fig. 8(a), (c) and (d), respectively), the 0.2 M-C samples exhibited the highest nesquehonite intensity, followed by the 0.1 M-C samples, while nesquehonite was negligible in the C-C sample. This trend suggests that L-Asp promotes nesquehonite formation. During the decomposition of nesquehonite to hydromagnesite, dypingite was

formed as an intermediate phase. The transition caused the loss of CO<sub>2</sub> and water [54]. Therefore, this particular hydrated magnesium carbonate (i.e. nesquehonite) sequestered more CO<sub>2</sub> than the other carbonates, such as dypingite. Similar biomimetic interactions between negatively charged amino acids and calcium carbonate solutions stabilised otherwise unstable carbonates [37,38,40,45]. This is comparable to the stabilisation of nesquehonite, a relatively unstable magnesium carbonate. Moreover, the impact of L-Asp occurred immediately after one day and continued for 14 days without signs of decomposition of nesquehonite into other more stable carbonates, such as the primary carbonate dypingite found in the control sample. The immediate impact of L-Asp will be discussed later.

However, an anomaly occurred at 3 days (Fig. 8(b)), where the 0.1 M-C sample exhibited a more intense nesquehonite peak than the 0.2 M-C sample. This deviation coincides with a brucite spike, in contrast to the patterns at 1, 7 and 14 days, where brucite peaks at 19° and 38° 2θ were negligible. Over time, the nesquehonite intensity of the 0.1 M-C sample declined relative to the 0.2 M-C sample, where nesquehonite intensity remained significantly higher at 14 days (Fig. 8(d)). Furthermore, the 0.1 M-C sample exhibited a higher brucite peak than the control sample, which had the highest brucite peak at 14 days, followed by the C-C sample. The distinctive break-in pattern was not observed in the control sample at any curing age, suggesting that L-Asp influenced MgO hydration and brucite carbonation, with its concentration affecting the timing of these processes. Higher L-Asp concentrations accelerated carbonation, aligning with the trends observed in Fig. 5.

It is worth noting here that, in the 0.2 M-C sample, the periclase peak at 37°, 43° 2θ had the highest intensity across all curing ages, indicating a greater amount of unreacted MgO. This suggests that a higher L-Asp concentration reduced hydration, consistent with the findings in Section 3.1. This high amount of unreacted MgO in the 0.2 M-C sample also demonstrated potential for further carbonation over time, leading to continuous strength gain through CO<sub>2</sub> sequestration. Meanwhile, the control sample had the lowest periclase content after 1 day, but by 3 and 14 days of curing, the 0.1 M-C sample exhibited the lowest periclase content, aligning with the C-C sample by day 14, suggesting that L-Asp only reduced hydration when it had a higher concentration (i.e. 0.2 M). Alternatively, a sample at a lower concentration of 0.1 M exhibited that its hydration was not too dissimilar to that of the C-C sample, which also agrees well with the XRD patterns of hydrated samples (Fig. 2). Furthermore, a substantial amount of unreacted MgO persisted in all samples, in contrast to ambient-cured samples, where MgO was almost entirely hydrated after 14 days. This indicates that carbonation inhibited MgO hydration, as carbonation products coated unreacted MgO particles, reducing their exposure to reactive conditions [34,55,56].

### 3.2.4. TG/DTG

In this study, TG was employed to quantify the amount of CO<sub>2</sub> absorbed by the binders after 14 days of carbonation curing, thereby evaluating the sequestration potential of MgO as a cementitious material under various concentrations of L-Asp. Fig. 9 presents the TG and DTG curves for all samples after 14 days of carbonation curing. The sample containing 0.2 M L-Asp exhibited the highest total mass loss (i.e. 42.7 %), indicating the highest reaction degree among all groups. However, this value was only slightly higher than that of the 0.1 M-C samples (38.4 %), indicating that a significant amount of unreacted MgO remained even at higher L-Asp concentrations. The third stage (i.e. from 540 to 900 °C) of mass loss (as shown in Table 2) in the 0.2 M-C sample was 7.6 %, which was higher than that of the 0.1 M-C samples (6.0 %), suggesting a higher presence of carbonate phases in the 0.2 M-C samples. The TG results illustrate mass loss over specific temperature ranges through the sequential release of water from the HMCs, dehydroxylation of brucite and HMCs (the release of hydroxyl functional group through water), and the decarbonation of HMCs. These processes are represented by three distinct mass loss stages in Fig. 9. However, the second slope, which exhibited the largest drop in mass, represents an overlap of

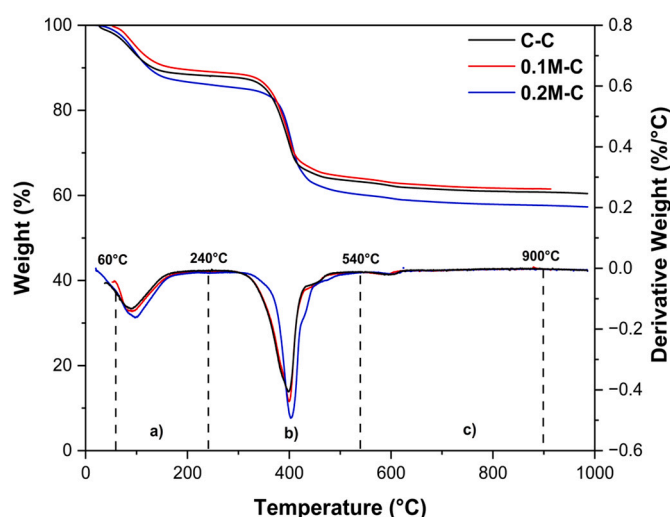


Fig. 9. Thermogravimetric analysis of all samples after 14 days of CO<sub>2</sub> curing

Table 2

Mass loss of carbonated samples obtained by TG-DTG after 14 days of carbonation.

Sample	Dehydration (%)	Dehydroxylation (%)	Decarbonation (%)	R <sub>CO2</sub> (%)
C-C	11.4	22.6	5.5	9.1
0.1M-C	11.4	21.0	6.0	9.7
0.2M-C	15.2	19.9	7.6	13.2

brucite dehydroxylation, HMC dehydroxylation, and partial HMC decarbonation, as these processes occur over similar temperature ranges [57,58]. To better differentiate these stages, the TG curves were analysed in terms of temperature derivatives, producing three peaks in the DTG curves shown in Fig. 9. The decomposition temperatures of each phase were determined from the endothermic peaks in the DTG curves, with the area under each peak corresponding to the respective weight loss. The three primary decomposition steps observed in all samples are summarised as follows [58–61]:

- 60 to 240 °C: Dehydration of water bonded to HMCs, such as nesquehonite (MgCO<sub>3</sub>•3H<sub>2</sub>O) and dypingite (4MgCO<sub>3</sub>•Mg(OH)<sub>2</sub>•5H<sub>2</sub>O);
- 240 to 540 °C: Decomposition of uncarbonated brucite, dehydroxylation of HMCs (e.g. dypingite (4MgCO<sub>3</sub>•Mg(OH)<sub>2</sub>•5H<sub>2</sub>O) and decarbonation of HMCs (e.g. nesquehonite (MgCO<sub>3</sub>•3H<sub>2</sub>O)); and
- 540 to 900 °C: Complete decarbonation of HMCs.

As shown in Fig. 9, the 0.2 M-C sample exhibited a peak shift at 400 °C, which was higher than that of the control and the 0.1 M-C samples (390 °C), suggesting that the hydroxyl functional group in both brucite and the HMCs had a stronger bond, requiring more energy for decomposition. A similar shift was observed in the water molecules associated with the HMCs, such as nesquehonite and dypingite, which were identified in the XRD results (Fig. 8). The 0.1 M-C sample also exhibited a smaller peak shift, indicating a trend where increasing L-Asp concentrations led to stronger carbonate bonds. This observation aligns with FTIR results discussed in the next section, where less stable carbonates transformed into more stable forms, and transformation was delayed in L-Asp-containing samples.

### 3.2.5. Phase quantifications from DTG

The DTG curves were deconvoluted using the Gaussian area deconvolution method to quantify the amount of water and CO<sub>2</sub> released

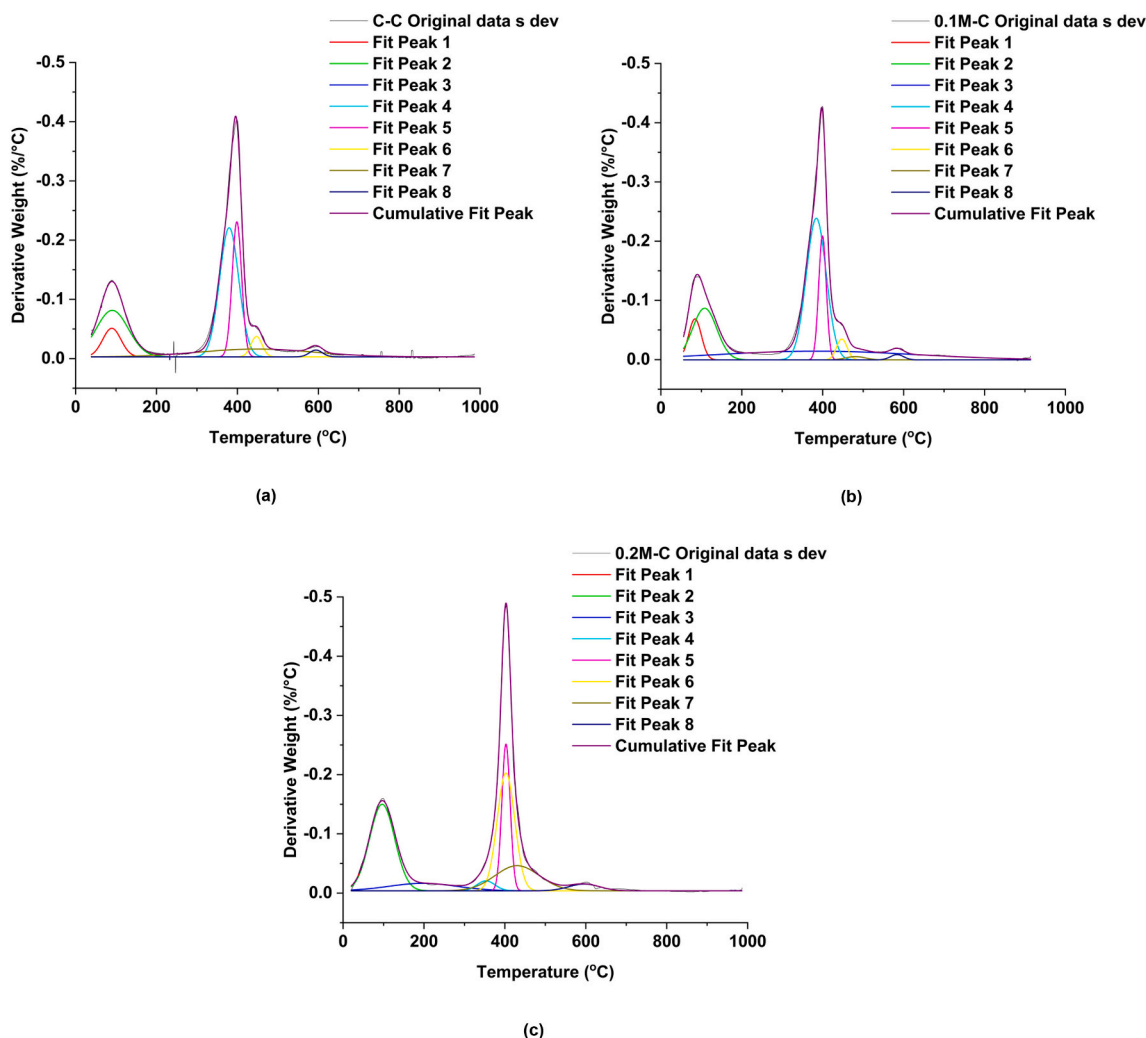


Fig. 10. Deconvoluted DTG curves of (a) C-C, (b) 0.1 M-C, and (c) 0.2 M-C samples at 14 days.

during thermal decomposition at each stage of the process. Fig. 10 presents the deconvoluted DTG curves for all samples cured for 14 days. For each sample, the original data were included in the plots with the cumulative fit (represented by the purple lines), formed by the combination of all deconvoluted curves. Distinct decomposition reactions are identified by their corresponding deconvoluted curves. For example, two curves (Fit Peaks 1 and 2) were used to represent the dehydration of adsorbed water and the loss of bonded water in HMCs within the C-C, 0.1 M-C and 0.2 M-C samples, as described in Eq. (10). The light blue and pink curves (Fit Peaks 4 and 5), centred around  $\sim 400$  °C, correspond to the dehydroxylation of brucite in all samples. Fit Peak 4 represents the decomposition of brucite within the formed HMC (i.e. dypingite) to MgO, shown in Eq. (11), while Fit peak 5 primarily corresponds to the decomposition of the uncarbonated brucite to MgO (Eq. (12)). Finally, the decomposition of magnesium carbonate to MgO is characterised by Fit Peaks 6–8 (Eq. (13)) [58]. Compared to the C-C and 0.1 M-C samples, which required three curves to represent HMC dehydration, the 0.2 M-C sample exhibited only two curves. This reduction suggests a higher degree of HMC formation within this sample, indicating that its primary weight loss is attributed to HMC dehydration.

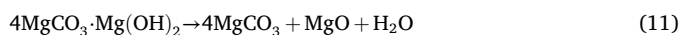
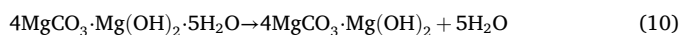


Table 2 presents the mass loss associated with each decomposition process, determined by calculating the area under the corresponding deconvoluted DTG curves (Fig. 10). Due to the significant overlap in the dehydroxylation temperature of brucite and the decarbonation/dehydroxylation of HMCs (ranging from 240 to 540 °C), isolating the effect of L-Asp on the quantity of brucite and HMCs is challenging. However, the impact of L-Asp is evident in the decarbonation mass loss, which was up to 38 % higher in the sample containing 0.2 M L-Asp compared to the control batch (7.6 % vs. 5.5 %, see Table 2). The highest dehydration (15.2 %) and decarbonation (7.6 %) mass loss observed in the 0.2 M-C sample indicates the highest yield of HMCs. Interestingly, this result deviates from theoretical expectations; if dypingite were the predominant carbonate phase in the C-C sample, a higher bound water content would be expected due to its crystalline water structure. However, the C-C sample exhibited the lowest dehydration (11.4 %) and decarbonation (5.5 %) loss, indicating a lower bound water content, consequently, a reduced HMC content. In terms of dehydroxylation, the C-C sample exhibited the highest weight loss (22.6 %) owing to the highest amount of brucite content. Although the 0.1 M-C sample showed a slightly lower weight loss (21 %) within the 240–540 °C range, XRD patterns (Fig. 8) confirm a higher brucite content than the C-C sample. This discrepancy suggests that the majority of HMCs in the C-C sample were dypingite, which contained oxhydril groups, while nesquehonite, which lacks oxhydril group, exhibits higher weight loss because of the

dehydroxylation. The CO<sub>2</sub> sequestration capacity of the sample was evaluated using the CO<sub>2</sub> sequestration ratio ( $R_{CO_2}$ ), calculated according to Eq. (14), where  $P_{CO_2}$  represents the percentage of CO<sub>2</sub> sequestered, and  $P_{MgO}$  denotes the percentage of residual MgO mass at 900 °C. As shown in Table 2, CO<sub>2</sub> capture increased in the presence of L-Asp, demonstrating its influence on the sequestration process.

$$R_{CO_2} = P_{CO_2}/P_{MgO} \quad (14)$$

### 3.2.6. FTIR analysis

The FTIR spectra of the MgO samples subjected to accelerated carbonation with varying concentrations of L-Asp are presented in Fig. 11, after 1, 3, 7 and 14 days of curing. These spectra were used to identify characteristic bonds corresponding to HMCs, as summarised in Table 3. Notably, the higher the intensity of the bands (i.e. higher transmittance), the higher the bond strength, consequently the higher amounts of the associated phase.

Key absorption bands observed at 3700 cm<sup>-1</sup>, 1650 cm<sup>-1</sup>, 1420–1480 cm<sup>-1</sup>, 1094 cm<sup>-1</sup>, 850 cm<sup>-1</sup> and 2750–3500 cm<sup>-1</sup> persisted across all curing stages and amino acid concentrations, though with varying intensities. The magnesium atom in brucite was positioned in an octahedral configuration with its hydroxyl ligands, where hydroxyl ions occupied C<sub>3v</sub> sites, generating a strong IR band at 3700 cm<sup>-1</sup> because of the antisymmetric O-H stretching vibrations. Additionally, the bands at 1420 cm<sup>-1</sup>, persisted in all samples across all curing ages, were not a single symmetrical peak but rather a combination of multiple hydrated

**Table 3**

Wavenumbers (cm<sup>-1</sup>) of FTIR absorption peaks for different HMC polymorphs.

Band position (cm <sup>-1</sup> )	Origin	Movement
3700	Brucite (Mg(OH) <sub>2</sub> )	Asymmetrical stretching OH bond [63,64]
1740	C=O unknown	Unknown [65]
1650	H <sub>2</sub> O from HMC	Bending vibration of H-O-H bonds [64,66]
1420–1480	CO <sub>3</sub> <sup>2-</sup> from HMC	v <sub>3</sub> asymmetric stretching vibration [18,63]
1380 (shoulder)	CO <sub>3</sub> <sup>2-</sup> from HMC	Vibration [63,67]
1223	C=O unknown	Unknown [65]
1094	CO <sub>3</sub> <sup>2-</sup> from nesquehonite	v <sub>1</sub> symmetric stretching mode [68,69]
850	CO <sub>3</sub> <sup>2-</sup> from HMC	Bending vibrations [63,70]
2750–3500 (broad)	Water of crystallisation	Bending vibration of H-O-H bonds [63,66]

magnesium carbonate phases in an asymmetric band. These carbonation products were corroborated by XRD results in Fig. 11(a) to (d), where they are nesquehonite and dypingite at 29.5° 2θ for all samples across all curing ages.

Two unidentified absorption bands at 1740 cm<sup>-1</sup> and 1223 cm<sup>-1</sup> were detected in all samples after 1 day of curing but disappeared for the C-C sample after 3 days. Additionally, these bands were absent for the 0.2 M-C and 0.1 M-C samples after 7 days. Although these peaks are

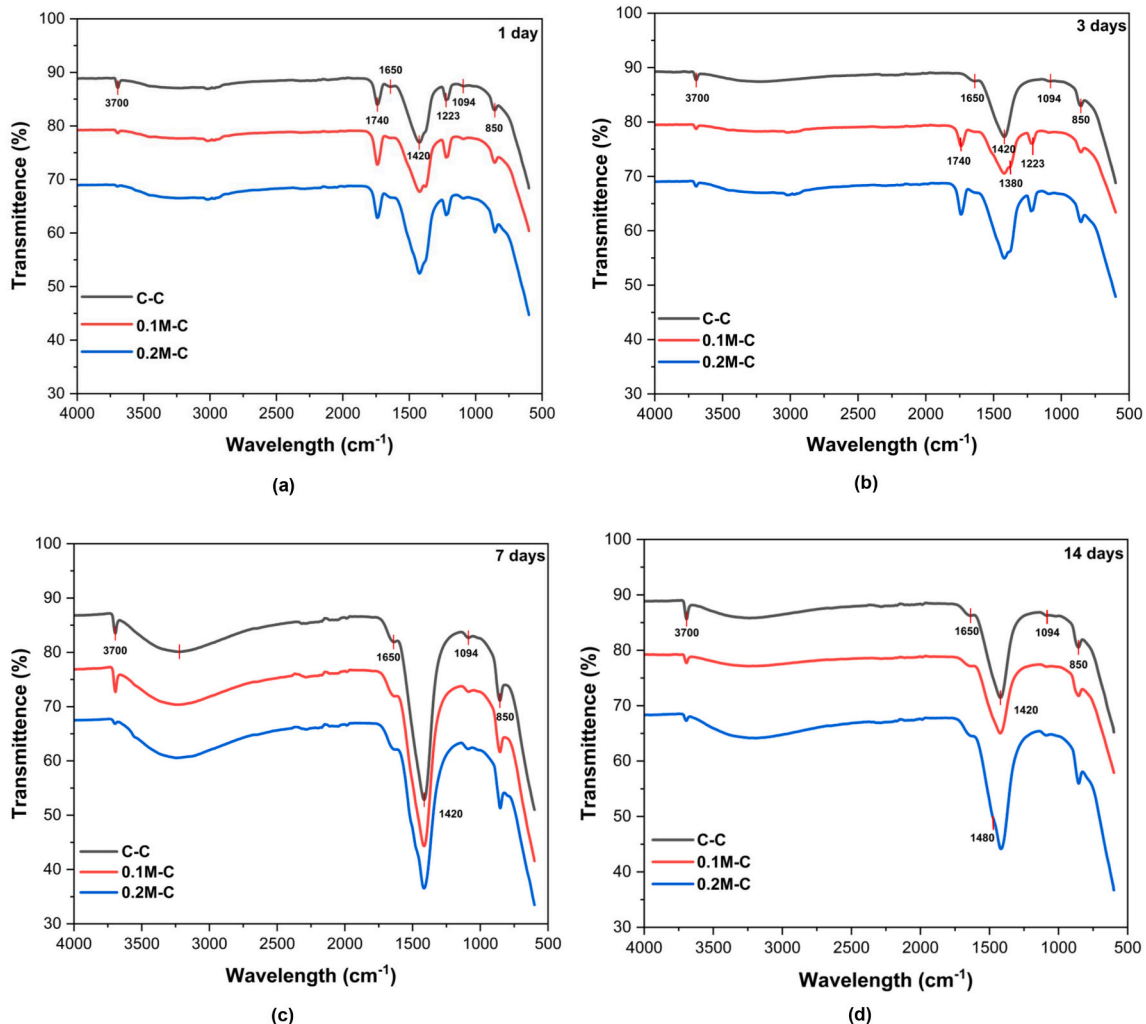


**Fig. 11.** FTIR spectra of all samples subjected to CO<sub>2</sub> curing for (a) 1, (b) 3, (c) 7, and (d) 14 days.

typically associated with a double bond between a carbon and oxygen atom (C=O) in various molecular structures [62], their precise origin remains unclear. However, given that they were absent in the control sample (C-C), they are unlikely to be linked to L-Asp, despite the presence of a carbonyl functional group in the amino acid. Therefore, the only alternative would be to associate this double bond between carbon and oxygen with the carbonate ions in hydrated magnesium carbonates. This interpretation is further supported by the corresponding XRD data presented in Fig. 8(a) to (d).

A similar pattern was observed in the shoulder at  $1380\text{ cm}^{-1}$  on the right side of  $1420\text{ cm}^{-1}$ . However, the difference is that these bands were identifiable, as referenced in Table 3, as carbonate ions associated with magnesium carbonates. Simultaneously, a shoulder appeared on the left side of the same band corresponding to  $1480\text{ cm}^{-1}$ , another carbonate ion associated with magnesium carbonate. The overall observation suggests that all samples followed an orderly transformation pattern; however, there was a delay in the occurrence of these bands shifting in the presence of amino acids. To summarise, L-Asp may have a stabilising effect on the relatively unstable carbonate phases that were short-lived, aligning with the XRD results. However, the concentration effect cannot be discerned since both 0.2 M-C and 0.1 M-C samples shifted bands simultaneously. To further investigate potential concentration-dependent effects, testing samples cured for between 1 and 7 days may provide additional insights. As discussed in Section 3.2.3, there was a discrepancy in the pattern that resulted in diminished nesquehonite peaks and elevated brucite peaks dependent on the concentration of L-Asp, which may be linked to these FTIR peak shifts.

### 3.2.7. SEM

Fig. 12 presents the microstructures of all samples after 14 days of carbonation, in which Fig. 12(a) reveals a sparse microstructure of the C-C sample observed by SEM, with several unhydrated MgO grains, consistent with XRD and TG results. The formation of large rosette-like crystals within a porous microstructure, as shown in Fig. 12(a), demonstrates the morphology of the HMCs in the C-C samples. Compared with the C-C samples, it can be seen that L-Asp improved the morphology of hydration and carbonation products through the densification of the microstructure, as observed in Fig. 12(b) and (c). Notably, L-Asp induced a remarkable transition in HMC polymorphs, shifting from rosette-like crystal agglomerates to needle-like nesquehonite crystals. Additionally, compared to the C-C sample, which demonstrated a higher crystalline degree, the samples containing L-Asp exhibited a higher proportion of amorphous phases, highlighting the ability of L-Asp to regulate polymorph formation and inhibit excessive crystallisation.

The effect of L-Asp concentration on microstructure development is evident in Fig. 12(b) and (c). The 0.2 M-C sample exhibited a denser microstructure compared to the 0.1 M-C sample, correlating with its higher nesquehonite content, which is also in line with the TG results. The needle-like nesquehonite crystals in the 0.2 M-C sample were agglomerated and surrounded by other phases, contributing to microstructure densification. The agglomeration of needle-like nesquehonite is likely due to nucleation effects induced by L-Asp, facilitating the growth and organisation of nesquehonite crystals. Overall, the addition of L-Asp had a beneficial impact on the microstructure and morphology of the carbonation products, which resulted in a denser microstructure and favourable HMC polymorphs toward enhanced mechanical properties. The improved microstructure and morphology are expected to

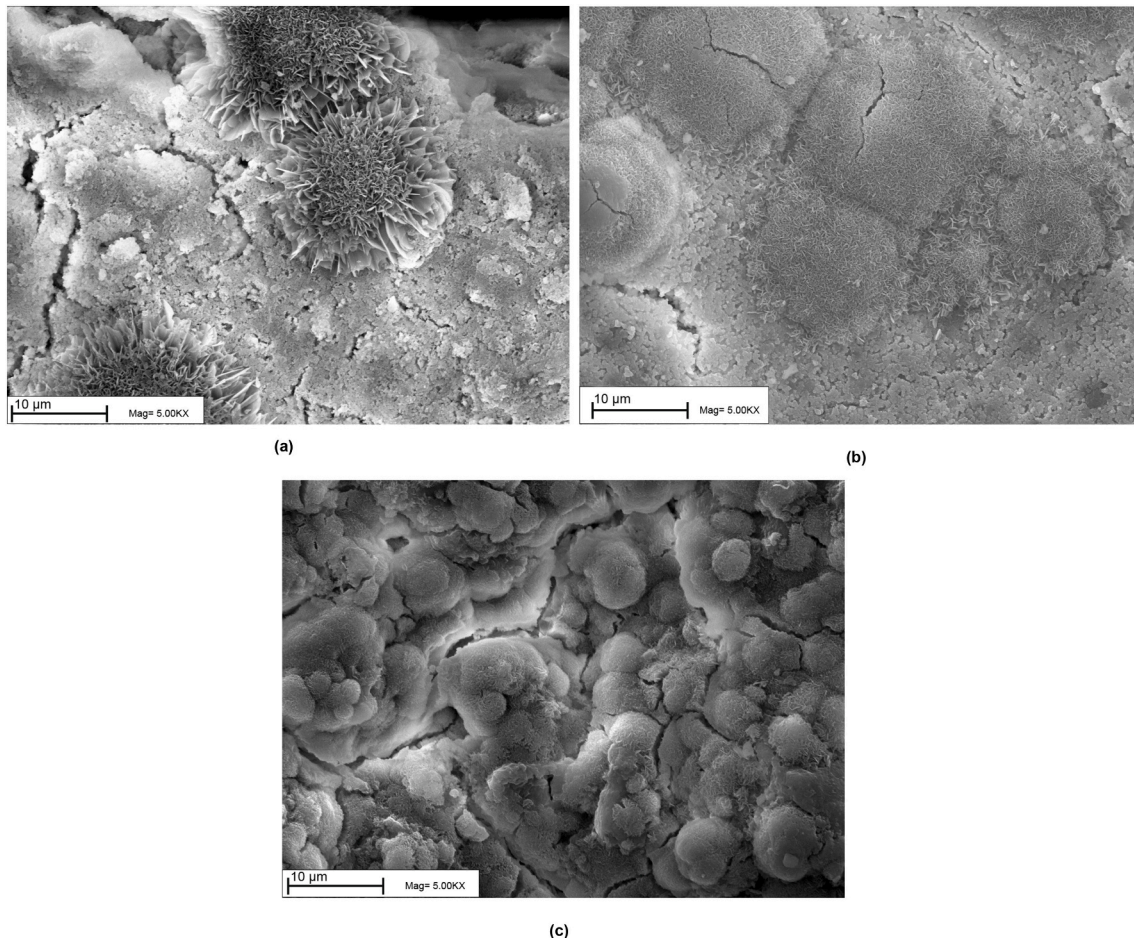


Fig. 12. SEM images of MgO with/without L-Asp after 14 days of accelerated carbonation curing: (a) C-C; (b) 0.1 M-C; and (c) 0.2 M-C.

correlate with increased strength and durability, making L-Asp a promising additive for optimising carbonation-based materials.

#### 4. Discussion

The stability of magnesium carbonates (Mg-carbonates) increases as they transition from more to less hydrated phases in the following order: nesquehonite < dypingite < hydromagnesite < magnesite [71]. According to Ostwald's step rule, a less stable polymorph crystallises first, making nesquehonite the primary carbonation product of MgO. However, the presence of L-Asp, either dissolved in solution or adsorbed on nesquehonite surfaces, stabilises this phase and delays its transformation into more stable carbonates [38,72]. In this way, because of the stabilisation of a particular metastable polymorphic phase, the Ostwald step sequence was halted at an intermediate stage. Amino acids were amphoteric substances, and their isoelectric point ( $pI$ ) was the pH of the solution when they were in an isoelectric state. Amino acids exist primarily as anions at  $pH >$  their  $pI$ , while at  $pH <$  their  $pI$ , they are predominantly cationic. The  $pI$  of L-Asp was 2.77, which is much lower than the highly alkaline MgO-binder environment (usually  $pH >$  10.5), based on the theory of electrostatic interaction and charge matching [73]. The schematic diagram to demonstrate the formation of hydration and carbonation products in magnesia with and without amino acids is illustrated in Fig. 13. When L-Asp reaches supersaturation, a strong attraction exists between the excess negative charge of L-Asp and  $Mg^{2+}$ ,

enhancing ion concentration and promoting carbonate precipitation. This mechanism may explain the outstanding performance-controlling effects observed at higher L-Asp concentrations. Moreover, the double negatively charged carboxyl groups in L-Asp bind to specific crystal planes, inhibiting excessive crystal growth [40,73]. This process likely contributes to the formation of amorphous brucite, as confirmed in Fig. 8. Additionally, carbon dioxide is another by-product during oxidative deamination of amino acids, which dissolves at elevated pH to form  $HCO_3^-$  or  $CO_3^{2-}$  [74], which subsequently can provide more reactants to produce HMCs. The proposed mechanism of amino acid-assisted carbonation of MgO is illustrated in Fig. 13.

##### 4.1. Impact of L-Asp on strength and microstructure

The accelerated dissolution of MgO by amino acids promotes carbonation, which subsequently enhances strength development. Amino acids become highly negatively charged when the pH is greater than their isoelectric point, attracting  $Mg^{2+}$  ions, resulting in increased ion concentration and promoting carbonate precipitation, which eventually leads to greater hydration and carbonation, and then a higher strength. As a result, carbonation products are more uniformly dispersed within the binder, preventing MgO particle encapsulation. This dispersion increases the exposure of unreacted MgO to  $H_2O$  and  $CO_2$ , thereby enhancing the carbonation degree and contributing to higher compressive strength and a denser microstructure in the material.

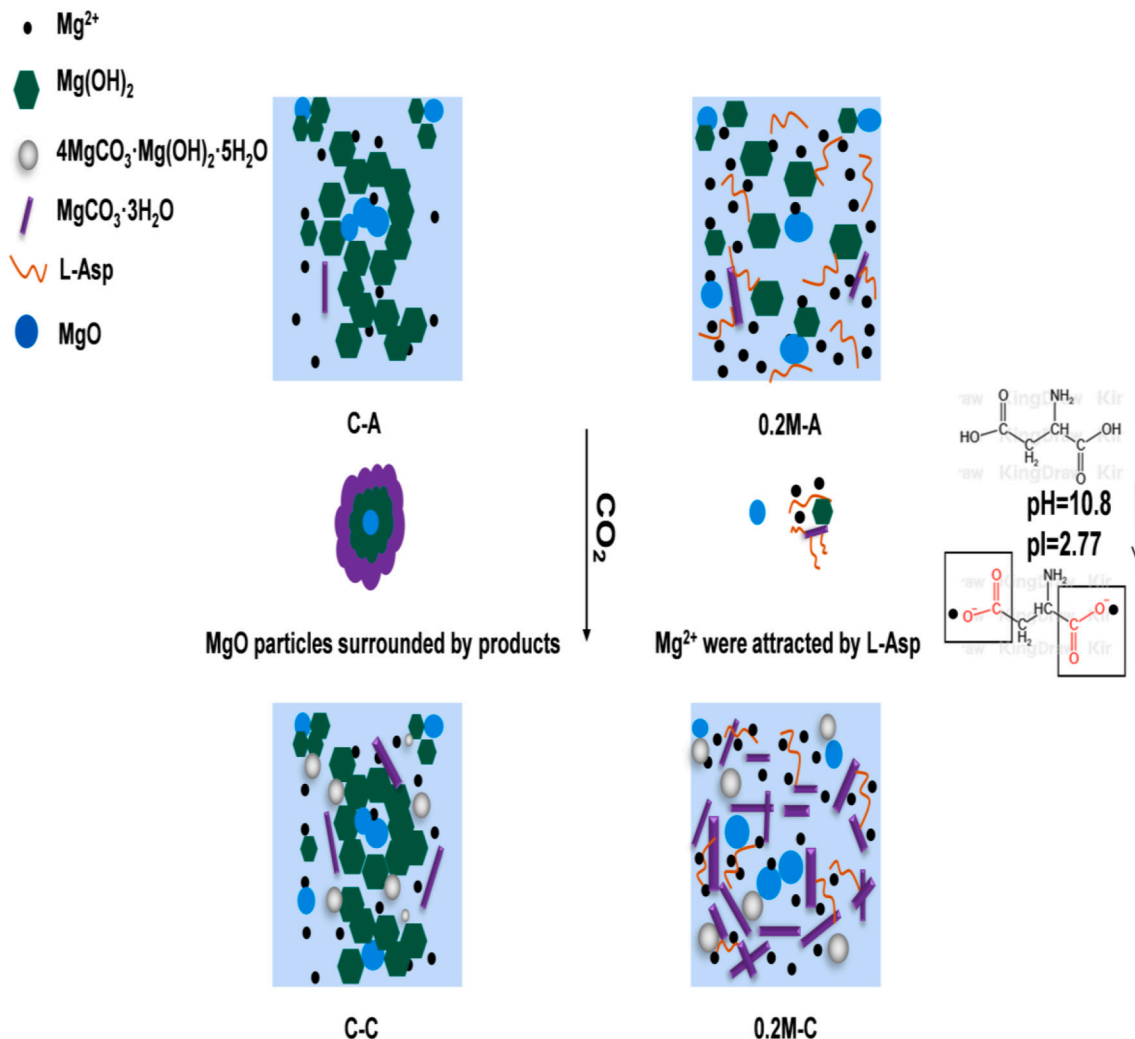


Fig. 13. Mechanism of synergistic hydration and carbonation in MgO composites with L-Asp.

#### 4.2. CO<sub>2</sub> sequestration performance enhanced by L-Asp

The improved carbon absorption ability was a highlighted benefit of the incorporation of L-Asp. In this study, the amount of absorbed CO<sub>2</sub> was also calculated, according to the thermogravimetric analysis (Table 2). C-C sample captured 5.5 wt% CO<sub>2</sub> of the total binder mass, with 60.5 wt% unreacted MgO. Therefore, 1 t of plain MgO can capture 90 kg of CO<sub>2</sub> after 14 days of CO<sub>2</sub> curing. When 0.2 M L-Asp was added to the binder, the captured CO<sub>2</sub> increased to 7.6 wt% of the total binder mass, consequently, 1 t of MgO with 0.2 M L-Asp can absorb 132 kg of CO<sub>2</sub> after 14 days of CO<sub>2</sub> curing, which is 46.7 % higher than that of the C-A binder without L-Asp. Given that the CO<sub>2</sub> sequestration capacity of HMCs is reported to be 300–500 kg CO<sub>2</sub> per tonne [75–77], the MgO-L-Asp composite can achieve approximately 26.4 % of its maximum CO<sub>2</sub> absorption within 14 days of CO<sub>2</sub> curing, demonstrating promising performance. Additionally, if MgO-L-Asp is fully carbonated, it is estimated to sequester approximately 1.09 t of CO<sub>2</sub> per tonne of MgO. This highlights the potential for further research into achieving full carbonation of MgO in the presence of organic compounds, a topic of state-of-the-art importance.

#### 4.3. Influence of L-Asp on amorphous phases and mechanical properties

Beyond polymorph controlling effects, L-Asp also demonstrated the impact on the amorphousness of the reaction products and their microstructure (as shown in Figs. 8 and 12). This study found that the amorphousness of the reaction products can affect the mechanical properties of the MgO-based binders. Higher amorphousness leads to higher reactivity of the products, which broadens the potential applications of these materials.

#### 5. Conclusions

This study investigated the impact of negatively charged L-aspartic (L-Asp) on the hydration and carbonation of reactive magnesia (RM) and explored its role in controlling the crystallisation of hydrated magnesium carbonates (HMCs) in carbonation-cured MgO. Hardened properties, including bulk density and compressive strength, of hydrated and carbonated reactive MgO composites with and without L-Asp were investigated. In addition, TG/DTG, ICP-OES, FTIR, XRD and SEM were employed to provide a thorough understanding of the performance of MgO-L-Asp composites. Based on the findings of this research, the following conclusions can be drawn:

- L-Asp not only decelerated the hydration of MgO but also reduced the formation of hydration products (i.e. brucite), leading to the lowest brucite content in L-Asp-containing samples. However, L-Asp promoted the formation of brucite with poor crystallinity, which, despite its reduced quantity, enhanced strength development due to its higher amorphous content. Simultaneously, the increased Mg<sup>2+</sup> concentration in solution resulted in a higher carbonation degree. Even though L-Asp reduced the amount of hydration phase, it led to the formation of crystalline brucite with high amorphousness, which has a positive contribution to strength gain.
- With the addition of L-Asp, MgO composites can absorb more CO<sub>2</sub>. For instance, the 0.2 M-C sample sequestered 46.7 % more CO<sub>2</sub> than the C-C sample. Meanwhile, amino acids improved the stabilisation of nesquehonite, the primary HMC polymorph, in carbonated MgO composites, further enhancing carbonation degree, with its effectiveness increasing at higher L-Asp concentrations.
- The MgO-H<sub>2</sub>O composites containing 0.2 M L-Asp exhibited a 16 % and 34.2 %, respectively, increase in compressive strength after 14 days of ambient curing and CO<sub>2</sub> curing, compared to the control one. The 0.2 M-C mixtures not only achieved higher compressive strength but also captured more CO<sub>2</sub>. Therefore, MgO-L-Asp composites are more sustainable binders than plain MgO mixtures.

- L-Asp altered the hydration product's morphology and densified the magnesia-based composites' microstructure. The morphology of hydration products plays a more important role in strength gain than the quantity of hydration products, reinforcing the role of microstructure refinement in improving mechanical properties.
- L-Asp retarded the precipitation of Mg<sup>2+</sup> and OH<sup>-</sup>. Consequently, L-Asp-containing samples had higher concentrations of Mg<sup>2+</sup> and OH<sup>-</sup> than the control sample, suggesting that L-Asp has the potential to improve the carbonation of MgO.
- The impact of L-Asp on hydration and carbonation is influenced by the pH–isoelectric point (pI) gap. A greater pH–pI gap enhances MgO dissolution, leading to higher hydration and carbonation degrees, and ultimately, greater strength development.

Overall, this study highlights the potential of L-Asp as a sustainable additive for improving MgO-based binders, offering enhanced mechanical performance, increased CO<sub>2</sub> sequestration, and controlled crystallisation of HMCs. Further research into the long-term stability and full carbonation potential of MgO–L-Asp composites is recommended to optimise their application in carbon-neutral construction materials.

#### CRediT authorship contribution statement

**Shuang Liang:** Writing – original draft, Visualization, Validation, Methodology, Investigation, Formal analysis, Data curation. **Xiangming Zhou:** Writing – review & editing, Supervision, Resources, Project administration, Methodology, Funding acquisition, Conceptualization. **Pengkun Hou:** Validation, Supervision, Methodology, Formal analysis, Conceptualization.

#### Declaration of competing interest

The authors declare that they have no known competing financial interests or personal relationships that could have appeared to influence the work reported in this paper.

#### Acknowledgement

The authors would like to thank the financial support from UKRI under grant EP/X04145X/1 (i.e., the CSTO2NE project) and the European Commission under grant 893469 (i.e. the NEASCMS project). The first author would also like to thank Zhongyuan University of Technology for providing a partial PhD scholarship to him to proceed with this study at Brunel University London.

#### Data availability

Data will be made available on request.

#### References

- [1] E. Benhelal, G. Zahedi, E. Shamsaei, A. Bahadori, Global strategies and potentials to curb CO<sub>2</sub> emissions in cement industry, *J. Clean. Prod.* 51 (2013) 142–161, <https://doi.org/10.1016/j.jclepro.2012.10.049>.
- [2] J. An, R.S. Middleton, Y. Li, Environmental performance analysis of cement production with CO<sub>2</sub> capture and storage technology in a life-cycle perspective, *Sustainability* 11 (2019), <https://doi.org/10.3390/su11092626>.
- [3] World Business Council for Sustainable Development, *The cement sustainability initiative: getting the numbers right*, 2009.
- [4] A. Al-Tabbaa, Reactive Magnesia Cement, Anonymous Eco-Efficient Concrete, Elsevier, in, 2013, pp. 523–543, <https://doi.org/10.1533/9780857098993.4.523>.
- [5] K. Hirota, N. Okabayashi, K. Toyoda, O. Yamaguchi, Characterization and sintering of reactive MgO, *Mater. Res. Bull.* 27 (1992) 319–326, [https://doi.org/10.1016/0025-5408\(92\)90061-4](https://doi.org/10.1016/0025-5408(92)90061-4).
- [6] A. Fabbri, J. Corvisier, A. Schubnel, F. Brunet, B. Goffé, G. Rimmele, V. Barlet-Gouédard, Effect of carbonation on the hydro-mechanical properties of Portland cements, *Cem. Concr. Res.* 39 (2009) 1156–1163, <https://doi.org/10.1016/j.cemconres.2009.07.028>.

- [7] G. Rimmelé, V. Barlet-Gouédard, O. Porcherie, B. Goffé, F. Brunet, Heterogeneous porosity distribution in Portland cement exposed to CO<sub>2</sub>-rich fluids, *Cem. Concr. Res.* 38 (2008) 1038–1048, <https://doi.org/10.1016/j.cemconres.2008.03.022>.
- [8] H.F. Taylor, *Cement chemistry*, Thomas Telford, London, 1997.
- [9] G.W. Groves, D.I. Rodway, I.G. Richardson, The carbonation of hardened cement pastes, *Adv. Cement Res.* 3 (1990) 117–125, <https://doi.org/10.1680/adcr.1990.3.11.117>.
- [10] P.D. Silva, L. Buceca, V. Sirivivatnanon, Chemical, microstructural and strength development of calcium and magnesium carbonate binders, *Cem. Concr. Res.* 39 (2009) 460–465, <https://doi.org/10.1016/j.cemconres.2009.02.003>.
- [11] C. Unluer, *Enhancing the carbonation of reactive magnesia cement-based porous blocks*, diss. university of Cambridge, 2012.
- [12] S.A. Walling, J.L. Provis, Magnesia-based cements: a journey of 150 years, and cements for the future? *Chem. Rev.* 116 (2016) 4170–4204, <https://doi.org/10.1021/acs.chemrev.5b00463>.
- [13] M. Liska, L.J. Vandeperre, A. Al-Tabbaa, Influence of carbonation on the properties of reactive magnesia cement-based pressed masonry units, *Adv. Cement Res.* 20 (2008) 53–64, <https://doi.org/10.1680/adcr.2008.20.2.53>.
- [14] D. Wang, J. Zhu, F. He, CO<sub>2</sub> carbonation-induced improvement in strength and microstructure of reactive MgO-CaO-fly ash-solidified soils, *Construct. Build Mater.* 229 (2019) 116914, <https://doi.org/10.1016/j.conbuildmat.2019.116914>.
- [15] M. Liska, A. Al-Tabbaa, Performance of magnesia cements in porous blocks in acid and magnesium environments, *Adv. Cement Res.* 24 (2012) 221–232, <https://doi.org/10.1680/adcr.11.00011>.
- [16] M. Liska, A. Al-Tabbaa, Ultra-green construction: reactive magnesia masonry products, *Proceedings of the institution of civil engineers-waste and resource management*. 162 (2009) 185–196, <https://doi.org/10.1680/warm.2009.162.4.185>.
- [17] L.J. Vandeperre, A. Al-Tabbaa, Accelerated carbonation of reactive MgO cements, *Adv. Cement Res.* 19 (2007) 67–79, <https://doi.org/10.1680/adcr.2007.19.2.67>.
- [18] N.T. Dung, C. Unluer, Carbonated MgO concrete with improved performance: the influence of temperature and hydration agent on hydration, carbonation and strength gain, *Cem. Concr. Compos.* 82 (2017) 152–164, <https://doi.org/10.1016/j.cemconcomp.2017.06.006>.
- [19] L. Pu, C. Unluer, Effect of preconditioning on carbonated reactive MgO-based concrete samples, *J. Mater. Civ. Eng.* 32 (2020) 04020314, [https://doi.org/10.1061/\(ASCE\)MT.1943-5533.0003416](https://doi.org/10.1061/(ASCE)MT.1943-5533.0003416).
- [20] L. Pu, C. Unluer, Performance and microstructure of carbonated MgO samples under high temperatures, *J. Mater. Civ. Eng.* 31 (2019) 04019003, [https://doi.org/10.1061/\(ASCE\)MT.1943-5533.0002624](https://doi.org/10.1061/(ASCE)MT.1943-5533.0002624).
- [21] C. Unluer, A. Al-Tabbaa, Enhancing the carbonation of MgO cement porous blocks through improved curing conditions, *Cem. Concr. Res.* 59 (2014) 55–65, <https://doi.org/10.1016/j.cemconres.2014.02.005>.
- [22] L. Wang, L. Chen, J.L. Provis, D.C. Tsang, C.S. Poon, Accelerated carbonation of reactive MgO and Portland cement blends under flowing CO<sub>2</sub> gas, *Cem. Concr. Compos.* 106 (2020) 103489, <https://doi.org/10.1016/j.cemconcomp.2019.103489>.
- [23] L. Pu, C. Unluer, Investigation of carbonation depth and its influence on the performance and microstructure of MgO cement and PC mixes, *Construct. Build Mater.* 120 (2016) 349–363, <https://doi.org/10.1016/j.conbuildmat.2016.05.067>.
- [24] N.T. Dung, R. Hay, A. Lesimple, K. Celik, C. Unluer, Influence of CO<sub>2</sub> concentration on the performance of MgO cement mixes, *Cem. Concr. Compos.* 115 (2021) 103826, <https://doi.org/10.1016/j.cemconcomp.2020.103826>.
- [25] R. Hay, K. Celik, Accelerated carbonation of reactive magnesium oxide cement (RMC)-based composite with supercritical carbon dioxide (scCO<sub>2</sub>), *J. Clean. Prod.* 248 (2020) 119282, <https://doi.org/10.1016/j.jclepro.2019.119282>.
- [26] L. Mo, F. Zhang, M. Deng, D.K. Panesar, Effectiveness of using CO<sub>2</sub> pressure to enhance the carbonation of Portland cement-fly ash-MgO mortars, *Cem. Concr. Compos.* 70 (2016) 78–85, <https://doi.org/10.1016/j.cemconcomp.2016.03.013>.
- [27] K. Rausis, A. Ćwik, I. Casanova, Phase evolution during accelerated CO<sub>2</sub> mineralization of brucite under concentrated CO<sub>2</sub> and simulated flue gas conditions, *J. CO<sub>2</sub> Util.* 37 (2020) 122–133, <https://doi.org/10.1016/j.jcou.2019.12.007>.
- [28] S. Ruan, C. Unluer, Effect of air entrainment on the performance of reactive MgO and PC mixes, *Construct. Build Mater.* 142 (2017) 221–232, <https://doi.org/10.1016/j.conbuildmat.2017.03.068>.
- [29] R. Hay, K. Celik, Hydration, carbonation, strength development and corrosion resistance of reactive MgO cement-based composites, *Cem. Concr. Res.* 128 (2020) 105941, <https://doi.org/10.1016/j.cemconres.2019.105941>.
- [30] C. Unluer, A. Al-Tabbaa, *Effect of Aggregate Size Distribution on the Carbonation of Reactive Magnesia Based Porous Blocks*, 18th Annual International Sustainable Development Research Conference, Hull, UK, 2012.
- [31] S. Liang, X. Zhou, P. Hou, Impact of amino acids as performance-controlling additives on the hydration of reactive MgO, *J. Phys.: Conf. Ser.* 2423 (2023) 12029, <https://doi.org/10.1088/1742-6596/2423/1/012029>.
- [32] D. Langmuir, Stability of carbonates in the system MgO-CO<sub>2</sub>-H<sub>2</sub>O, *J. Geol.* 73 (1965) 730–754, <https://doi.org/10.1086/627113>.
- [33] S.A. Wilson, M. Raudsepp, G.M. Dipple, Verifying and quantifying carbon fixation in minerals from serpentine-rich mine tailings using the Rietveld method with X-ray powder diffraction data, *Am. Mineral.* 91 (2006) 1331–1341, <https://doi.org/10.2138/am.2006.2058>.
- [34] A. Khalil, S. Sohn, K. Celik, Thermal properties and stability of reactive magnesia cement, *Constr. Build Mater.* 308 (2021) 125102, <https://doi.org/10.1016/j.conbuildmat.2021.125102>.
- [35] N.A.J.M. Sommerdijk, G.d. With, Biomimetic CaCO<sub>3</sub> mineralization using designer molecules and interfaces, *Chem. Rev.* 108 (2008) 4499–4550, <https://doi.org/10.1021/cr078259o>.
- [36] L. Ma, J. Zhu, M. Cui, L. Huang, Biomimetic synthesis of novel calcium carbonate heterogeneous dendrites, *New J. Chem.* 39 (2015) 5309–5315, <https://doi.org/10.1039/C5NJ00219B>.
- [37] K. Maruyama, T. Yoshino, H. Kagi, Synthesizing a composite material of amorphous calcium carbonate and aspartic acid, *Mater. Lett.* 65 (2011) 179–181, <https://doi.org/10.1016/j.matlet.2010.09.039>.
- [38] Z. Zou, L. Bertinetti, Y. Politi, P. Fratzl, W.J. Habraken, Control of polymorph selection in amorphous calcium carbonate crystallization by poly (aspartic acid): two different mechanisms, *Small* 13 (2017) 1603100, <https://doi.org/10.1002/sml.201603100>.
- [39] R.I. Khan, W. Ashraf, J. Olek, Amino acids as performance-controlling additives in carbonation-activated cementitious materials, *Cem. Concr. Res.* 147 (2021) 106501, <https://doi.org/10.1016/j.cemconres.2021.106501>.
- [40] H. Tong, W. Ma, L. Wang, P. Wan, J. Hu, L. Cao, Control over the crystal phase, shape, size and aggregation of calcium carbonate via a L-aspartic acid inducing process, *Biomaterials* 25 (2004) 3923–3929, <https://doi.org/10.1016/j.biomaterials.2003.10.038>.
- [41] L. Štajner, J. Kontrec, B.N. Džakula, N. Maltar-Strmečki, M. Plodinec, D.M. Lyons, D. Kralj, The effect of different amino acids on spontaneous precipitation of calcium carbonate polymorphs, *J. Cryst. Growth* 486 (2018) 71–81, <https://doi.org/10.1016/j.jcrysgro.2018.01.023>.
- [42] P. Stempfle, O. Pantalé, R.K. Nijwa, M. Rousseau, E. Lopez, X. Bourrat, Friction-induced sheet nacre fracture: effects of nano-shocks on cracks location, *Int. J. Nanotechnol.* 4 (2007) 712–729, <https://doi.org/10.1504/IJNT.2007.015466>.
- [43] C.A. Orme, A. Noy, A. Wierzbicki, M.T. McBride, M. Grantham, H.H. Teng, P. M. Dove, J.J. DeYoreo, Formation of chiral morphologies through selective binding of amino acids to calcite surface steps, *Nature* 411 (2001) 775–779, <https://doi.org/10.1038/35081034>.
- [44] H.H. Teng, P.M. Dove, C.A. Orme, J.J. De Yoreo, Thermodynamics of calcite growth: baseline for understanding biomineral formation, *Science* 282 (1998) 724–727, <https://doi.org/10.1126/science.282.5389.724>.
- [45] Y. Kim, J.D. Carloni, B. Demarchi, D. Sparks, D.G. Reid, M.E. Kunitake, C.C. Tang, M.J. Duer, C.L. Freeman, B. Pokroy, Tuning hardness in calcite by incorporation of amino acids, *Nat. Mater.* 15 (2016) 903–910, <https://doi.org/10.1038/nmat4631>.
- [46] H. Wang, S. Liang, X. Zhou, P. Hou, X. Cheng, Regulating hydration and microstructure development of reactive MgO cement by citric acids, *Cem. Concr. Compos.* 155 (2025) 105832, <https://doi.org/10.1016/j.cemconcomp.2024.105832>.
- [47] H. Wang, T. Cai, S. Liang, P. Hou, Improving the hydration and carbonation of reactive MgO cement with amino acids and the influencing mechanisms, *J. Therm. Anal. Calorim.* (12) (2024) 1–12, <https://doi.org/10.1007/s10973-024-13092-w>.
- [48] *ASTM, Standard test methods for chemical analysis of limestone, quicklime, and hydrated lime*, 2011.
- [49] *ASTM, Standard test method for compressive strength of hydraulic cement mortars (using 2-in. or [50-mm] cube specimens)*, *Annual Book of ASTM Standards/Annual Book of ASTM Standards*. 4 (2013) 1–9.
- [50] S. Ma, A.H. Akca, D. Esposito, S. Kawashima, Influence of aqueous carbonate species on hydration and carbonation of reactive MgO cement, *J. CO<sub>2</sub> Util.* 41 (2020) 101260, <https://doi.org/10.1016/j.jcou.2020.101260>.
- [51] E.G. Soares, J. Castro-Gomes, M. Sitarz, T. Zdeb, I. Hager, K. Hassan, M.S. Al-Kuwari, Feasibility for co-utilisation of carbonated reactive magnesia cement (CRMC) and industrial wastes in circular economy and CO<sub>2</sub> mineralisation, *Constr. Build Mater.* 323 (2022) 126488, <https://doi.org/10.1016/j.conbuildmat.2022.126488>.
- [52] D.K. Panesar, L. Mo, Properties of binary and ternary reactive MgO mortar blends subjected to CO<sub>2</sub> curing, *Cem. Concr. Compos.* 38 (2013) 40–49, <https://doi.org/10.1016/j.cemconcomp.2013.03.009>.
- [53] S. Ruan, C. Unluer, Influence of mix design on the carbonation, mechanical properties and microstructure of reactive MgO cement-based concrete, *Cem. Concr. Compos.* 80 (2017) 104–114, <https://doi.org/10.1016/j.cemconcomp.2017.03.004>.
- [54] R. Chaliulina, J. Galvez-Martos, A. Hakki, A. Elhoweris, J. Mwanda, Y. Al-Horr, Eco materials from CO<sub>2</sub> capture: compressive strengths of a plasterboard alternative, *Construct. Build Mater.* 312 (2021) 125276, <https://doi.org/10.1016/j.conbuildmat.2021.125276>.
- [55] E.G. Soares, J. Castro-Gomes, Carbonation curing influencing factors of carbonated reactive magnesia cements (CRMC)—a review, *J. Clean. Prod.* 305 (2021) 127210, <https://doi.org/10.1016/j.jclepro.2021.127210>.
- [56] N.T. Dung, C. Unluer, Influence of nucleation seeding on the performance of carbonated MgO formulations, *Cem. Concr. Compos.* 83 (2017) 1–9, <https://doi.org/10.1016/j.cemconcomp.2017.07.005>.
- [57] R. Hay, N.T. Dung, A. Lesimple, C. Unluer, K. Celik, Mechanical and microstructural changes in reactive magnesium oxide cement-based concrete mixes subjected to high temperatures, *Cem. Concr. Compos.* 118 (2021) 103955, <https://doi.org/10.1016/j.cemconcomp.2021.103955>.
- [58] C. Unluer, A. Al-Tabbaa, Impact of hydrated magnesium carbonate additives on the carbonation of reactive MgO cements, *Cem. Concr. Res.* 54 (2013) 87–97, <https://doi.org/10.1016/j.cemconres.2013.08.009>.
- [59] N.T. Dung, A. Lesimple, R. Hay, K. Celik, C. Unluer, Formation of carbonate phases and their effect on the performance of reactive MgO cement formulations, *Cem. Concr. Res.* 125 (2019) 105894, <https://doi.org/10.1016/j.cemconres.2019.105894>.

- [60] H. Nguyen, H. Santos, H. Sreenivasan, W. Kunther, V. Carvelli, M. Illikainen, P. Kinnunen, On the carbonation of brucite: effects of mg-acetate on the precipitation of hydrated magnesium carbonates in aqueous environment, *Cem. Concr. Res.* 153 (2022) 106696, <https://doi.org/10.1016/j.cemconres.2021.106696>.
- [61] G. Jauffret, J. Morrison, F.P. Glasser, On the thermal decomposition of nesquehonite, *J. Therm. Anal. Calorim.* 122 (2015) 601–609, <https://doi.org/10.1007/s10973-015-4756-0>.
- [62] G. Socrates, *Infrared and raman characteristic group frequencies: tables and charts*, John Wiley & Sons, 2004.
- [63] C. Kuenzel, F. Zhang, V. Ferrandiz-Mas, C.R. Cheeseman, E.M. Gartner, The mechanism of hydration of MgO-hydromagnesite blends, *Cem. Concr. Res.* 103 (2018) 123–129, <https://doi.org/10.1016/j.cemconres.2017.10.003>.
- [64] G.B. Singh, C. Sonat, E.H. Yang, C. Unluer, Performance of MgO and MgO-SiO<sub>2</sub> systems containing seeds under different curing conditions, *Cem. Concr. Compos.* 108 (2020) 103543, <https://doi.org/10.1016/j.cemconcomp.2020.103543>.
- [65] V. Țucureanu, A. Matei, A.M. Avram, FTIR spectroscopy for carbon family study, *Crit. Rev. Anal. Chem.* 46 (6) (2016) 502–520, <https://doi.org/10.1080/10408347.2016.1157013>.
- [66] H.A. Abdel-Gawwad, S.A. El-Enein, M. Heikal, S. Abd El-Aleem, A.A. Amer, I.M. El-Kattan, Synergistic effects of curing conditions and magnesium oxide addition on the physico-mechanical properties and firing resistivity of Portland cement mortar, *Construct. Build Mater.* 176 (2018) 676–689, <https://doi.org/10.1016/j.conbuildmat.2018.05.092>.
- [67] A. Ansari, A. Ali, M. Asif, Microwave-assisted MgO NP catalyzed one-pot multicomponent synthesis of polysubstituted steroidal pyridines, *New J. Chem.* 42 (2018) 184–197, <https://doi.org/10.1039/C7NJ03742B>.
- [68] R.L. Frost, S. Bahfenne, Raman and mid-IR spectroscopic study of the magnesium carbonate minerals—brugnatellite and coalingite, *J. Raman Spectrosc.* 40 (2009) 360–365, <https://doi.org/10.1002/jrs.2110>.
- [69] H.G. Edwards, S.E.J. Villar, J. Jehlicka, T. Munshi, FT-Raman spectroscopic study of calcium-rich and magnesium-rich carbonate minerals, *pectrochim. Acta, Part A.* 61 (2005) 2273–2280, <https://doi.org/10.1016/j.saa.2005.02.026>.
- [70] H. Han, S. Hu, J. Feng, H. Gao, Effect of stearic acid, zinc stearate coating on the properties of synthetic hydromagnesite, *Appl. Surf. Sci.* 257 (2011) 2677–2682, <https://doi.org/10.1016/j.apsusc.2010.10.041>.
- [71] A.L. Harrison, V. Mavromatis, E.H. Oelkers, P. Bénéžeth, Solubility of the hydrated mg-carbonates nesquehonite and dypingite from 5 to 35 °C: implications for CO<sub>2</sub> storage and the relative stability of mg-carbonates, *Chem. Geol.* 504 (2019) 123–135, <https://doi.org/10.1016/j.chemgeo.2018.11.003>.
- [72] A. Rodriguez-navarro, C. Jimenez-lopez, A. Checa, J.M.G. Ruiz, Nanocrystalline structures in calcium carbonate biominerals, *J. Nanophoton.* (2008), <https://doi.org/10.1117/1.3062826>.
- [73] A. Xie, Y. Shen, C. Zhang, Z. Yuan, X. Zhu, Y. Yang, Crystal growth of calcium carbonate with various morphologies in different amino acid systems, *J. Cryst. Growth* 285 (2005) 436–443, <https://doi.org/10.1016/j.jcrysgro.2005.08.039>.
- [74] C. Rodriguez-Navarro, M. Rodriguez-Gallego, K. Ben Chekroun, M.T. Gonzalez-Muñoz, Conservation of ornamental stone by *Myxococcus xanthus*-induced carbonate biomineralization, *Appl. Environ. Microbiol.* 69 (2003) 2182–2193, <https://doi.org/10.1128/AEM.69.4.2182-2193.2003>.
- [75] R. Zhang, A. Arrigoni, D.K. Panesar, Could reactive MgO cement be a green solution? The effect of CO<sub>2</sub> mineralization and manufacturing route on the potential global warming impact, *Cem. Concr. Compos.* 124 (2021) 104263, <https://doi.org/10.1016/j.cemconcomp.2021.104263>.
- [76] S. Ruan, C. Unluer, Comparative life cycle assessment of reactive MgO and Portland cement production, *J. Clean. Prod.* 137 (2016) 258–273, <https://doi.org/10.1016/j.jclepro.2016.07.071>.
- [77] C. Unluer, Carbon dioxide sequestration in magnesium-based binders, in: *Anonymous Carbon Dioxide Sequestration in Cementitious Construction Materials*, Elsevier, 2018, pp. 129–173, <https://doi.org/10.1016/B978-0-08-102444-7.00007-1>.